

Earth and Space Science



RESEARCH ARTICLE

10.1029/2023EA003007

Key Points:

- Applicability of four long-term terrestrial water storage anomaly data sets is assessed using two completely independent tests
- Abnormally, terrestrial water storage anomalies of two subbasins have almost no correlation with El Niño-Southern Oscillation (ENSO)
- This abnormality is dominated by regional precipitation's weak link with ENSO

Supporting Information:

Supporting Information may be found in the online version of this article.

Correspondence to:

T. Jin,
tyjin@sgg.whu.edu.cn

Citation:

Li, X., Jin, T., Liu, B., Chao, N., Li, F., & Cai, Z. (2023). The influence of ENSO on the long-term water storage anomalies in the Middle-Lower reaches of the Yangtze River basin: Evaluation and analysis. *Earth and Space Science*, 10, e2023EA003007. <https://doi.org/10.1029/2023EA003007>

Received 3 MAY 2023
Accepted 11 SEP 2023

Author Contributions:

Conceptualization: Taoyong Jin
Data curation: Xiaolong Li
Formal analysis: Xiaolong Li, Bingshi Liu
Funding acquisition: Taoyong Jin
Investigation: Taoyong Jin, Bingshi Liu, Nengfang Chao, Fupeng Li, Zuansi Cai
Methodology: Xiaolong Li
Project Administration: Taoyong Jin
Resources: Xiaolong Li, Bingshi Liu
Software: Xiaolong Li
Supervision: Taoyong Jin, Nengfang Chao, Fupeng Li, Zuansi Cai
Validation: Taoyong Jin

© 2023 The Authors.

This is an open access article under the terms of the [Creative Commons Attribution-NonCommercial License](https://creativecommons.org/licenses/by-nc/4.0/), which permits use, distribution and reproduction in any medium, provided the original work is properly cited and is not used for commercial purposes.

The Influence of ENSO on the Long-Term Water Storage Anomalies in the Middle-Lower Reaches of the Yangtze River Basin: Evaluation and Analysis

Xiaolong Li¹ , Taoyong Jin^{1,2} , Bingshi Liu¹ , Nengfang Chao³ , Fupeng Li⁴, and Zuansi Cai⁵ 

¹School of Geodesy and Geomatics, Hubei LuoJia Laboratory, Wuhan University, Wuhan, China, ²Key Laboratory of Geospace Environment and Geodesy, Ministry of Education, Wuhan, China, ³College of Marine Science and Technology, China University of Geosciences, Wuhan, China, ⁴Institute of Geodesy and Geoinformation, University of Bonn, Bonn, Germany, ⁵School of Computing, Engineering and the Built Environment, Edinburgh Napier University, Edinburgh, UK

Abstract Recent extreme events in the Middle-Lower reaches of the Yangtze River basin (MLYRB) are proven to be possibly linked to the El Niño-Southern Oscillation (ENSO) events as indicated by terrestrial water storage anomaly (TWSA). But the relatively short observation time of Gravity Recovery and Climate Experiment series missions (2002–2017; 2018–present) affects the robustness of the evaluation of TWSA. Here, the applicability of four long-term TWSA data sets (since 1979) in the MLYRB is evaluated first using an evaluation framework including two completely independent tests. After selecting the optimal one, we investigate the effects of ENSO on TWSA in the MLYRB at the basin, subbasin, and grid cell scales, respectively. Results show that ENSO, especially the Eastern Pacific type ENSO has had a significant impact on TWSA variations in the MLYRB and its two subbasins (the Dongting Lake basin and the Poyang Lake basin) since 1979 with correlation coefficients at 0.56–0.65 and time lags at 5–6 months. However, TWSAs in the other two subbasins (the Hanjiang River basin and the Mainstream River basin) have almost no correlation with ENSO. Further analysis reveals that compared with human activity that has a limited impact on TWSA, precipitation is one of the key inducements for regional water storage changes in these two subbasins, and the no correlation between ENSO and TWSA is mainly caused by the weak link between ENSO and precipitation.

1. Introduction

Since the last century, influenced by short and/or long-term climate fluctuations and human actions, the more frequent and severe water events, such as droughts, floods, and extreme rainfall have exacerbated global water insecurity and posed great challenges to global and regional water resources management (Dottori et al., 2018; Hinkel et al., 2014; IPCC, 2022; Kreibich et al., 2022). Among them, the El Niño-Southern Oscillation (ENSO), which is the largest signal in the interannual variation of the atmosphere-ocean system on periods ranging from about 2 to 7 years caused by sea surface temperature anomalies (SSTA) in the equatorial Pacific, has been shown to impact the frequency of droughts and floods significantly at a global scale (Dilley & Heyman, 1995; Emerton et al., 2017; Kao & Yu, 2009; Kug et al., 2009) and a regional scale, such as the California Coast (Andrews et al., 2004), the Ganges and Brahmaputra River basins (Pervez & Henebry, 2015), the Mekong River basin (Räsänen & Kumm, 2013), Papua New Guinea (Cobon et al., 2016), and the Middle-Lower reaches of the Yangtze River basin (MLYRB, Tong et al., 2006; Y. Yin et al., 2009).

As a major development area for China, the MLYRB has been suffering extreme water events that have proven to be related to ENSO events over the centuries, and seriously affect the located agricultural production and people's livelihoods (Ayantobo et al., 2022; Qi et al., 2022). Hence, effective monitoring of water extremes in the MLYRB and an attempt to obtain the impact of ENSO on these extremes is essential. Gravity Recovery and Climate Experiment (GRACE) satellite and its subsequent mission GRACE Follow-On (GRACE-FO) launched in March 2002 and May 2018, respectively, enable researchers to monitor water storage changes and identify water extremes efficiently and accurately over the past 20 years at a scale of about 20,000 km² (Chen et al., 2022; Rodell et al., 2018; Tapley et al., 2019). In practice, a large number of studies have shown that ENSO, especially the 2010–2011 La Niña and the 2015–2016 El Niño, is closely related to water extremes in the MLYRB in the past 20 years (Chen et al., 2022; Long et al., 2016; Reager et al., 2016; Rodell et al., 2018; Tapley et al., 2019; Z. Zhang et al., 2015; Zhao et al., 2017). However, the recording time of TWSA from GRACE and GRACE-FO (~20 years) is much shorter than that of ENSO (generally more than 40 years), which may lead to unreliable

Writing – original draft: Xiaolong Li, Bingshi Liu

Writing – review & editing: Xiaolong Li, Nengfang Chao, Fupeng Li, Zuansi Cai

results when making a correlation analysis between TWSA and ENSO. Hence, to increase confidence in the assessment this requires a longer record that extends prior to the GRACE period (i.e., before 2002). We define the TWSA data set with a recording time longer than GRACE as a long-term TWSA in this study.

Several studies have made great efforts to reconstruct the long-term TWSA series by establishing empirical statistical relationships between GRACE and climatic variables. These provide invaluable data sets to explore the long-term characteristics of water resource change, including the period prior to the GRACE era and/or assess the risk of extreme events (F. Li et al., 2021; D. Zhang et al., 2016). These statistical methods can be divided into component statistical models and overall statistical models. A component statistical model decomposes the GRACE TWSA series into multiple components. Then it reconstructs one/more components by establishing its/their relations with long-term climate indicators and adds these reconstructed components together to obtain the long-term TWSA finally (Humphrey et al., 2017; Humphrey & Gudmundsson, 2019a; F. Li et al., 2020, 2021). Instead of decomposing the GRACE TWSA into several components, an overall statistical model reconstructs the whole TWSA directly using GRACE and long-term climate indicators (Liu et al., 2021). In addition, global hydrological models, such as the WaterGAP Global Hydrology Model (WGHM), provide a long-term TWSA data set using a series of advanced numerical models (Döll et al., 2003). However, the applicability of these long-term TWSA data sets has not been sufficiently evaluated in the MLYRB. For example, Long et al. (2017) and Scanlon et al. (2018) assessed the performances of long-term TWSA products only from hydrological models, while Deng et al. (2023) evaluated the long-term TWSA products only derived only from statistical models. As a result, to avoid issues in applications such as data mismatch and data errors, the evaluation of these long-term TWSAs' performances in the MLYRB needs to be supplemented.

After the evaluation session, the goal of this study is to select the best-performing long-term TWSA and explore the impact of ENSO on the long-term TWSA in the MLYRB. However, though many studies have analyzed ENSO's impact on TWSA in the MLYRB, these studies have discussed either only at the basin scale (Ren et al., 2022; Wang et al., 2022; Z. Zhang et al., 2015) or only at the grid cell scale (Phillips et al., 2012; P. Yang et al., 2022), which probably lead to a lack of understanding of the relationship between TWSA and ENSO. Therefore, the correlation of TWSA and ENSO at multiple spatial scales (i.e., basin, subbasin, and grid cell) is necessary to be discussed and its spatial distribution difference needs to be explained.

Hence, this study aims to evaluate the performances of different long-term TWSAs in the MLYRB, analyze the multi-spatial scale effect of ENSO on long-term TWSA, and attempt to make an attribution analysis to the differences of spatial distribution. Data sets are outlined in Section 2, and methods used to evaluate the long-term TWSA and the impacts of ENSO events on TWSA are discussed in Section 3. Results of the evaluation of the long-term TWSA are shown and discussed in Section 4.1. Time-domain and frequency-domain correlations between the long-term TWSA and ENSO are described in Sections 4.2 and 4.3. In Section 4.4, we attempt to explain the spatial distribution regimes from the perspective of two key drivers: natural factors and human activities. The conclusion is presented in Section 5.

2. Data

2.1. Study Area

The Yangtze River, the longest river in China, runs from west to east across China, with a total length of approximately 6300 km before flowing into the East China sea in Shanghai. Taking Yichang and Hukou as the demarcation points, the Yangtze River is divided into upper, middle, and lower reaches. Since the ocean signals (e.g., ocean tide and storm tide) may cause massive uncertainty to the water level and discharge measurements in coastal regions, Datong station, located in Anhui Province with a distance to the estuary of the Yangtze River at about 624 km is regarded as the control station of the Yangtze River. In this study, we define region from Yichang to Datong as the MLYRB, and regions downstream of the Datong station are ignored (Figure 1a).

The MLYRB (24.49°N~34.20°N, 106.09°E~118.60°E) is about 7×10^5 km² and is mainly located in the subtropical monsoon region. Generally, the MLYRB can be divided into four subbasins: the Dongting Lake basin (DLB, controlled by Chenglingji station), the Hanjiang River basin (HRB, controlled by Xiantao station), the Mainstream River basin from Yichang to Datong (MRB, no control station) and the Poyang Lake basin (PLB, controlled by Hukou station) based on its hydrological systems shown in Figure 1a. Four hydrological stations' monthly average in-situ discharge regimes are characterized by a markedly unimodal cycle (Figure 1b). The

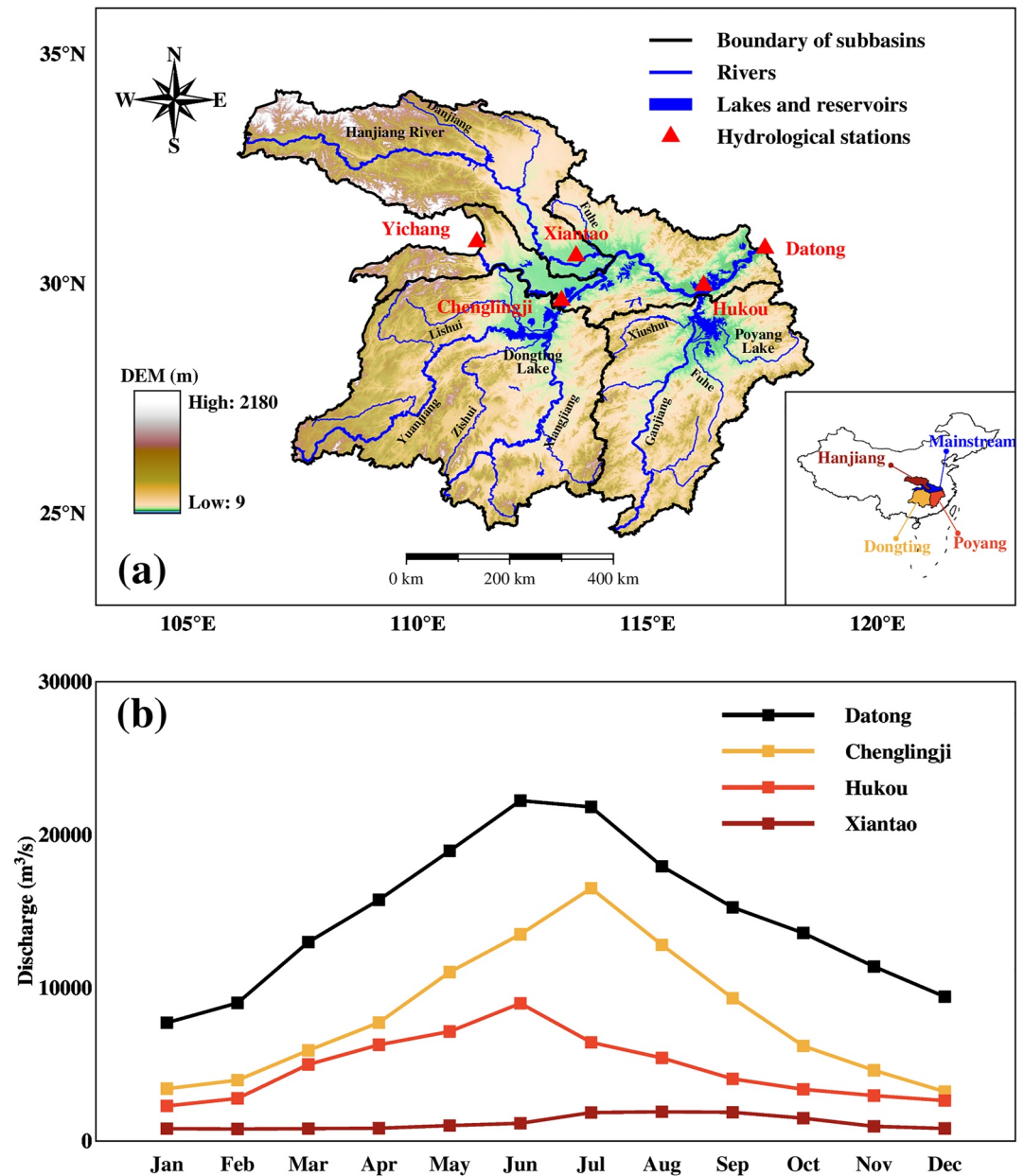


Figure 1. Location of the Middle-Lower reaches of the Yangtze River basin (MLYRB), subbasins, hydrological control stations, and monthly mean discharges of control stations. Datong, Chenglingji, Hukou, and Xiantao are control stations of the MLYRB, the Dongting Lake basin (DLB), the Poyang Lake basin (PLB), and the Hanjiang River basin (HRB), respectively.

difference is that the MLYRB and the PLB peak occur in June, while the DLB and the HRB peak in July and August, respectively. More information about the MLYRB and subbasins is shown in Table S1 in Supporting Information S1.

2.2. Terrestrial Water Storage Data

2.2.1. GRACE TWSA

In this study, two monthly RL06Mv2 GRACE and GRACE-FO mascon solutions released by the Center for Space Research (Save et al., 2016, abbreviated to CSR) and the Jet Propulsion Laboratory (Watkins et al., 2015, abbreviated to JPLM) cover from April 2002 to June 2017 and July 2018 to July 2022 are utilized to obtain TWSA

and make evaluation together with long-term TWSA data sets. The spatial resolution of CSRМ and JPLM are published as $0.25^\circ \times 0.25^\circ$ and $0.5^\circ \times 0.5^\circ$, respectively. The 11-month gap (July 2017 to June 2018) is caused by the delayed launch of the GRACE-FO mission.

2.2.2. Long-Term TWSA From Statistical Model and Global Hydrological Model

Four monthly long-term TWSA data sets: three from statistical models and one from global hydrological model are utilized:

1. The average of the six GRACE_REC_v03 data sets trained with GRACE GSFC mascon and JPLM solutions and forced with MSWEP, GSWP3, and ERA5 forcing (Humphrey & Gudmundsson, 2019a, abbreviated to HG19) with $0.5^\circ \times 0.5^\circ$ grids from 1901 to 2019.
2. The long-term gridded TWSA reconstructed based on CSRМ and dozens of climate inputs released by F. Li et al. (2021, abbreviated to Li21) with output grids of $0.5^\circ \times 0.5^\circ$ from 1979 to 2020.
3. The climate-driven water storage anomalies released by Liu et al. (2021, abbreviated to Liu21) driven by in-situ precipitation and temperature produced and forced by JPLM with $0.5^\circ \times 0.5^\circ$ globally grids from 1979 to 2021.
4. The long-term TWSA from WGHM 2.2d that was released by Müller Schmied et al. (2021) with $0.5^\circ \times 0.5^\circ$ cell grids from 1901 to 2016 are selected in this study (abbreviated to WGHM).

2.2.3. In-Situ Measured TWS

Except for TWSA products from satellite gravity and statistical models, yearly TWS (note that not the TWSA) data sets in the MLYRB and its four subbasins produced by the Changjiang Water Resources Commission of the Ministry of Water Resources (CWRC) from 2006 to 2021 are used to assess the yearly water storage change in the MLYRB and its subbasins in this study. The in-situ TWS released by CWRC is defined as the sum of surface runoff and the amount of groundwater replenishment by precipitation and surface water infiltration.

2.3. Water Balance Components Data

In order to assess the long-term TWSA, based on the water balance equation, a data set generated by precipitation, evapotranspiration, and river discharge from satellite and gauging stations is applied in this study. For more information about the water balance equation, please see Section 3.1.

We use monthly precipitation from four data sets: CRU TS 4.06 released by National Center for Atmospheric Research (New et al., 2000) from 1901 to 2021, ERA5 produced by European Center for Medium-Range Weather Forecasts (Hersbach et al., 2020) from 1950 to 2021, GPCC v2022 released by Deutscher Wetterdienst (Schneider et al., 2022) from 1891 to 2019, and U.Delaware V501 produced by University of Delaware (Willmott & Matsuura, 1995) from 1900 to 2017. This study uses two monthly evapotranspiration data sets: REA ET released by J. Lu et al. (2021a) from 1980 to 2017, and GLEAM v3.3a from 1980 to 2017 (Miralles et al., 2011). Monthly in-situ discharge data till 2021 of Datong, Chenglingji, Xiantao, and Hukou stations are available from CWRC.

2.4. Climate Index

In order to clarify the duration of the ENSO event and quantify its intensity, scholars usually generate ENSO indices from SSTA of the equatorial Pacific (Kao & Yu, 2009). In this study, the eastern Pacific type ENSO index (EPI) and the central Pacific type ENSO index (CPI) that characterizes ENSO events originating from SSTA of the eastern and central Pacific released by Sullivan et al. (2016) are utilized. The two indices are calculated from normalized Niño-3 and Niño-4 indices and cover 1854 to August 2021.

2.5. Human Water Use

2.5.1. Outputs of PCR-GLOBWB Model

This study uses the PCRaster Global Water Balance hydrological model (PCR-GLOBWB) to simulate long-term human water use outcomes (Cheng et al., 2021; Sutanudjaja et al., 2018; W. Yin et al., 2022). PCR-GLOBWB is an advanced grid-based global hydrology and water resources model released by Utrecht University. In the latest

version of PCR-GLOBWB 2.0, three types of human activities (i.e., non-irrigation water use, irrigation water use, and reservoir operation) are considered and fully integrated within the hydrological model. Human water use equals actual withdrawals from surface water (reservoirs, lakes, and rivers) and groundwater for industry, domestic, livestock, and irrigation. Numerous studies have confirmed the applicability of PCR-GLOBWB in the Yangtze River basin and China (Jiao et al., 2020; X. Yang et al., 2020).

Four 0.5-degree gridded components (i.e., industry, domestic, livestock, and irrigation water use) of monthly human water use simulated by PCR-GLOBWB 2.0 from 1960 to 2015 in the MLYRB are applied to evaluate the impact of human activities on regional water storage.

2.5.2. In-Situ Measurement of Water Diversion

As the largest inter-basin water diversion project in China, the South-to-North Water Diversion Project (SNWD) has transferred large amounts of fresh water from the Danjiangkou reservoir (starting point of the Central Route) and Jiangdu water conservancy hub (starting point of the Eastern Route) to North China since 2014. Due to the Danjiangkou reservoir located in the HRB, the impact of inter-basin water diversion on regional water storage must be addressed. Produced by CWRC, the yearly diversion quantity of the Central Route of the South-to-North Water Diversion Project (abbreviated to SNWD) during 2014 and 2021 are used in this study as a supplement to human water use. Please see Table 1 for more information of data sets used in this study.

3. Methods

3.1. Water Balance Equation

Water balance equation provides a completely independent method to assess the long-term TWSA using climatic data sets. For a given basin, the instantaneous equation of water balance equation (Scanlon et al., 2018):

$$\frac{dS}{dt} = P - ET - R \quad (1)$$

where P , ET , and R is precipitation, evapotranspiration, and runoff, respectively. $\frac{dS}{dt}$ means terrestrial water storage change (TWSC), that is defined as the difference between two successive months in TWSAs:

$$TWSC_{t_i} = TWSA_{t_{i+1}} - TWSA_{t_i} \quad (2)$$

where $TWSC_{t_i}$ and $TWSA_{t_i}$ mean TWSC and TWSA of month t_i ($i = 1, 2, 3, \dots, n$), respectively. We define TWSC from HG19, Li21, Liu21, and WGHM as HG19C, Li21C, Liu21C, and WGHMC, respectively.

3.2. Windowed Cross-Correlation (WCC) in the Time Domain

Pearson Correlation coefficient (CC) is used to assess the temporal correlation of yearly series. However, to obtain the time lag of TWSA in response to ENSO indices, we carry out the Windowed Cross-Correlation (WCC) at a 95% confidence level (Boker et al., 2002; Jammazi & Aloui, 2015):

$$r_k = \frac{\sum_{t=1}^{N-k} (x_t - \bar{x})(y_{t+k} - \bar{y})}{\sqrt{\sum_{t=1}^N (x_t - \bar{x})^2 \sum_{t=1}^N (y_t - \bar{y})^2}} \quad (3)$$

where x_t and y_t are time series with length N ; \bar{x} and \bar{y} mean average value of these two series. r_k represents the cross-correlation coefficient at time lag k ($k = 1, 2, 3, \dots, n$). Here, we regard ENSO indices as x_t and TWSA as y_t to explore the leading relationship between ENSO and TWSA.

Table 1
Summary of Data Sets Used in This Study

Source	Variable	Resolution		Time span	References
		Spatial	Temporal		
CSRM	TWSA	0.25°	Monthly	April 2002 to June 2017 June 2018 to July 2022	Save et al. (2016)
JPLM	TWSA	0.5°	Monthly	April 2002 to June 2017 June 2018 to July 2022	Watkins et al. (2015)
HG19	TWSA	0.5°	Monthly	January 1901 to June 2019	Humphrey and Gudmundsson (2019b)
L121	TWSA	0.5°	Monthly	July 1979 to June 2020	F. Li (2021)
Liu21	TWSA	0.5°	Monthly	January 1979 to December 2021	Liu et al. (2021)
WGHM	TWSA	0.5°	Monthly	January 1901 to December 2016	Döll et al. (2014)
CRU TS 4.06	<i>P</i>	0.5°	Monthly	January 1901 to December 2021	New et al. (2000)
ERA5	<i>P</i>	0.1°	Monthly	January 1950 to December 2021	Muñoz Sabater (2019)
GPCC v2022	<i>P</i>	0.5°	Monthly	January 1891 to December 2019	Schneider et al. (2020)
U-Delaware v501 ^a	<i>P</i>	0.5°	Monthly	January 1900 to December 2017	Willmott and Matsuura (1995)
REA ET	ET	0.25°	Monthly	January 1980 to December 2017	J. Lu et al. (2021b)
GLEAM v3.3a	ET	0.25°	Monthly	January 1980 to December 2018	Miralles et al. (2011)
CWRC ^b	<i>R</i>	Datong station ^c	Monthly	January 2000 to December 2021	Jin (2023)
	<i>R</i>	Chenglingji station ^c	Monthly	April 1991 to December 2021	Jin (2023)
	<i>R</i>	Xiantao station ^c	Monthly	January 1972 to December 2021	Jin (2023)
	<i>R</i>	Hukou station ^c	Monthly	January 2000 to December 2021	Jin (2023)
	TWS	/	Yearly	2006–2021	Jin (2023)
	Water diversion	SNWD	Yearly	2014–2021	Jin (2023)
PCR-GLOBWB 2.0	Human water use	0.5°	Monthly	January 1960 to December 2015	Sutanudjaja et al. (2017)

Note. Note that all gridded produces are interpolated to 0.5° grids using the two-dimensional cubic spline interpolation method (De Boor, 1978).

^aU-Delaware means the data sets produced by University of Delaware. ^bCWRC means Changjiang Water Resources Commission of the Ministry of Water Resources (website: <http://www.cjw.gov.cn/>). ^cDatong, Chenglingji, Xiantao, Hukou station are the control station of the MLYRB, the Dongting Lake basin (DLB), the Hanjiang River basin (HRB), and the Poyang Lake basin (PLB), respectively. Note that the Mainstream River basin from Yichang to Datong (MRB) has not control station.

3.3. Wavelet Coherence (WTC) in the Frequency Domain

Wavelet Coherence (WTC) has been a useful adaptive time-frequency analysis method for nonstationary signals (Fu et al., 2021; Rezaei & Gurdak, 2020; Su et al., 2019). As for series x_t and y_t , WTC could be defined as (Torrence & Compo, 1998):

$$R_n^2 = \frac{|S(s^{-1}W_i^{xy}(s))|^2}{S(s^{-1}|W_i^x|^2) \cdot S(s^{-1}|W_i^y|^2)} \quad (4)$$

in which $W_i^x(s)$ and $W_i^y(s)$ are wavelet transforms (Maraun & Kurths, 2004). S is the smooth operator depending on the wavelet type, and s is the wavelet scale. $W_i^{xy}(s)$ is defined as the following (Su et al., 2019):

$$W_i^{xy}(s) = W_i^x(s) \cdot W_i^{y*}(s) \quad (5)$$

here, $*$ means the complex conjugate. R_n^2 ranges from 0 to 1, representing the coherence of two series from no correlation to totally correlated. The phase angle of an arrow in a WTC map, which indicates the phase difference between two time series, enables us to obtain time lag between two time series using a conversion criterion Grinsted et al. (2004). For example, a phase arrow pointing right or left means the in-phase or anti-phase relationship between two time series.

3.4. Evaluation Metrics

CC, Nash-Sutcliffe efficiency (NSE), and root mean square error (RMSE) are utilized in this study to quantify the effect of the long-term TWSA. For two time series, CC indicates their relationship in phase, while NSE describes the matching of magnitude, phase, and bias between two series, and RMSE measures the deviation between them. These evaluation metrics are obtained as follows:

$$\left\{ \begin{array}{l} \text{CC} = \frac{\sum_{i=1}^n (O_i - \bar{O})(H_i - \bar{H})}{\sqrt{\sum_{i=1}^n (O_i - \bar{O})^2} \sqrt{\sum_{i=1}^n (H_i - \bar{H})^2}} \\ \text{NSE} = 1 - \frac{\sum_{i=1}^n (H_i - O_i)^2}{\sum_{i=1}^n (O_i - \bar{O})^2} \\ \text{RMSE} = \sqrt{\frac{1}{n} \sum_{i=1}^n (H_i - O_i)^2} \end{array} \right. \quad (6)$$

where H_i and O_i represent the long-term TWSA to be evaluated and data sets used to evaluate, respectively. n is the length of H_i and O_i . \bar{H} and \bar{O} are the mean value of H_i and O_i .

3.5. Pre-Process TWSA Before Correlation Analysis of ENSO

As mentioned in Jin et al. (2020) and Scanlon et al. (2019), TWSA can be decomposed into a linear trend, a seasonal component, an interannual component, and a high-frequency residual as the follows:

$$\text{TWSA}(\theta, \lambda, t) = a_0 + a_1 t + \sum_{i=1}^2 b_i \cos(2\pi f_i t + \varphi_i) + I_{\text{interannual}} + \text{residual} \quad (7)$$

where θ, λ are the colatitude and longitude, respectively; a_0 and a_1 are the offset and trend, respectively; b_i, f_i , and φ_i are amplitude, frequency, and initial phase of annual and semi-annual signals. $I_{\text{interannual}}$ mean the interannual component.

However, ENSO typically occurs every 3–5 years, and in the historical record, this interval has varied from 2 to 7 years, showing the periodic characteristics of low frequency (Chen et al., 2020). As a result, it is necessary to pre-process TWSA so that it has the same frequency band as ENSO to ensure the accuracy of correlation analysis. In this study, we remove the linear trend and the seasonal item from TWSA data sets using the least square method and then utilize a 13-month moving average filter to suppress the high-frequency residual (Jin et al., 2020).

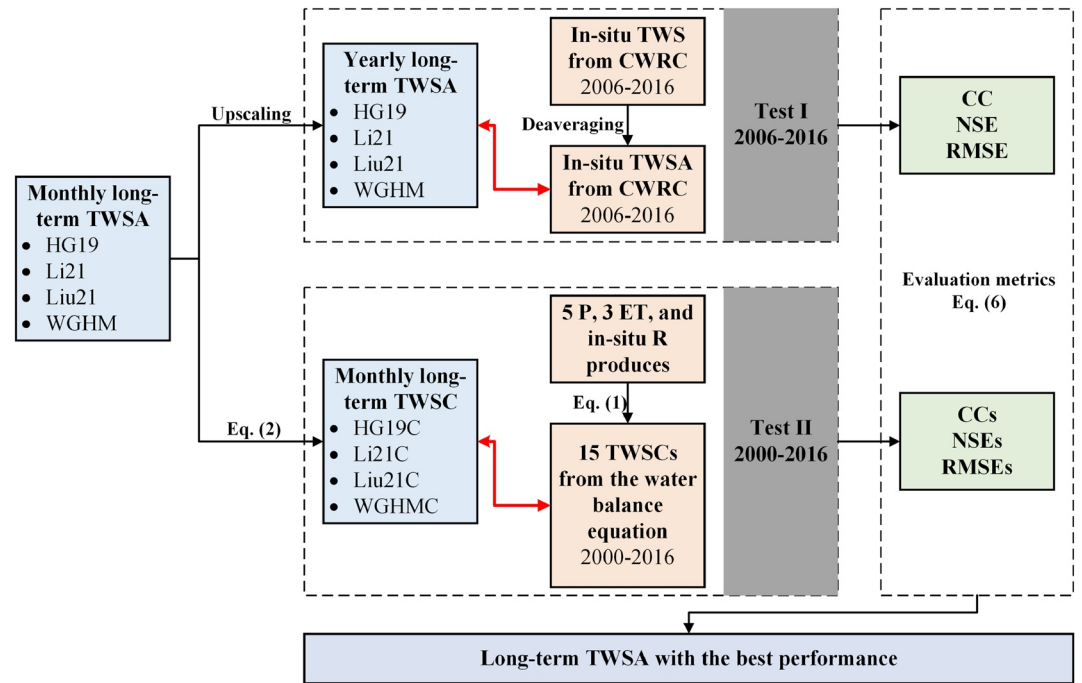


Figure 2. Flowchart of the framework for evaluating the long-term terrestrial water storage anomaly (TWSA). The evaluation time between the long-term TWSA and the in-situ TWSA is set from 2006 to 2016, while that between the long-term terrestrial water storage change (TWSC) and TWSCs from the water balance equation is set from 2000 to 2016.

3.6. Evaluating the Long-Term TWSA

To make the analysis concerning ENSO's impact on TWSA more realistic, it is one of the key steps to evaluate the performance of all of the long-term TWSAs and select the best-performing one in this manuscript. Here, we develop a framework that enables us to evaluate a long-term TWSA's performance in a specific basin using two completely independent data sets: the in-situ measured TWS in Section 2.2.3 and hydrometeorological data in Section 2.3 (Figure 2).

For example, when we attempt to evaluate long-term TWSAs' performance in the MLYRB, we would calculate as follows:

1. Obtain the in-situ TWS of the MLYRB from CWRC, and remove its mean value to obtain the in-situ TWSA series. At the same time, we upscale the monthly long-term TWSAs into annual ones. Calculate CCs, NSEs, and RMSEs between the annual long-term TWSAs and the annual in-situ TWSA.
2. Use Equation 2 to obtain the long-term TWSC, and obtain TWSC from the water balance equation by Equation 1. Note that in this study, TWSC from the water balance equation is a set of 15 members, which are permutations of 5 precipitation products (4 models and their average) and 3 evapotranspiration products (2 models and their average) that mentioned in Section 2.3. Calculate CCs, NSEs, and RMSEs between the long-term TWSC and TWSCs from the water balance equation.
3. Assess CCs, NSEs, and RMSEs from steps 1 and 2, and select the long-term TWSA with the best performance.

4. Results and Discussion

4.1. Evaluation of the Long-Term TWSA Data Sets

In this Section, we use the evaluation framework developed in Section 3.6 to evaluate four long-term TWSA's performance in the MLYRB and its four subbasins (i.e., the DLB, the HRB, the MRB, and the PLB). When making an assessment using in-situ measured TWS, we set the time period from 2006 to 2016. While for the assessment using the water balance equation, the time period is set from 2000 to 2016. Note that when we assess

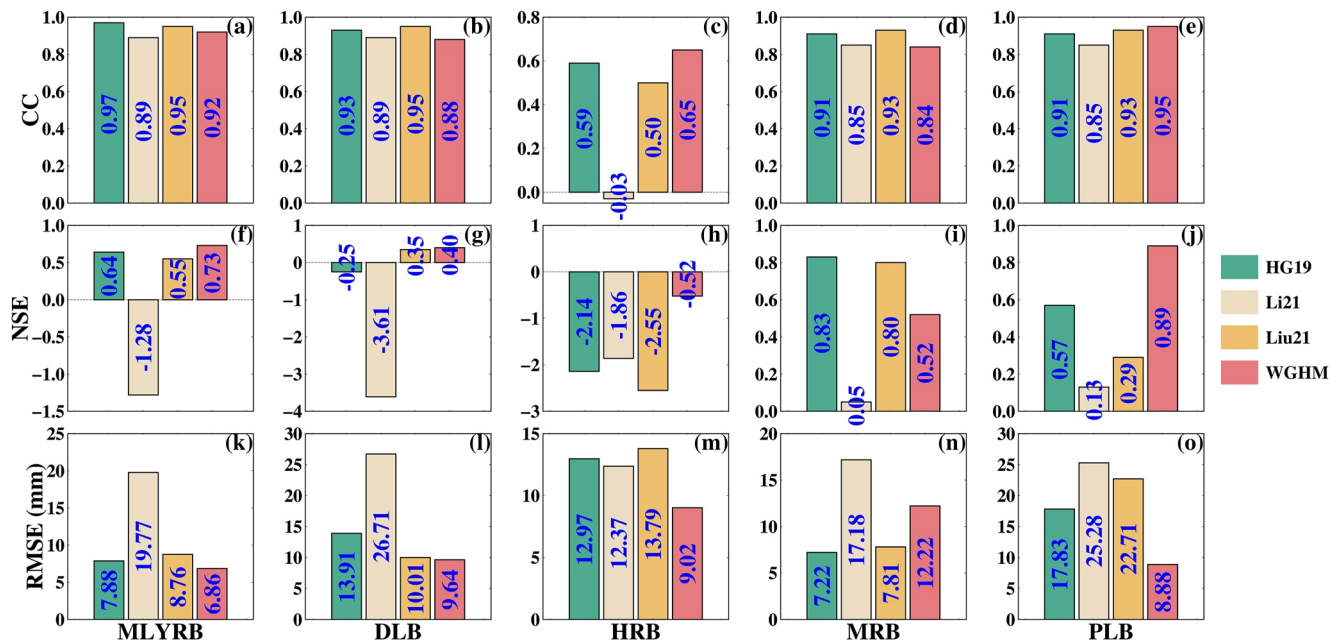


Figure 3. Comparison of Correlation coefficient (CC), Nash-Sutcliffe efficiency (NSE), and root mean square error (RMSE) between the long-term terrestrial water storage anomaly (TWSA) and the in-situ TWSA from 2006 to 2016 in the Middle-Lower reaches of the Yangtze River basin (MLYRB) and its four subbasins. Values are marked in blue. (a–e) The CC in the MLYRB and subbasins, (f–j) the NSE in the MLYRB and subbasins, and (k–o) the RMSE in the MLYRB and subbasins.

the long-term TWSA using the water balance equation, the MRB is excluded because it has no control station, which results in it having no runoff observations.

4.1.1. Test I: Evaluation Using the In-Situ TWS Measurements

CC, NSE, and RMSE between the long-term TWSA and the in-situ TWSA (the deaveraged in-situ TWS) in the MLYRB and its subbasins are shown in Figure 3 (series comparison of four long-term TWSA and the in-situ TWS please see Figure S1 in Supporting Information S1). It is clear that in the MLYRB, though HG19 has the largest CC (0.97) with the in-situ TWSA, WGHM has the largest NSE (0.73) and the smallest RMSE (6.86) with the in-situ TWSA (Figures 3a, 3f, and 3k). In Figures 3b–3e, we find that Liu21 (in the DLB and the MRB) and WGHM (in the HRB and the PLB) are more dominant in four subbasins. HG19 shows the largest NSE in the MRB, but it is WGHM that shows dominance in the NSE metric in the DLB, the HRB, and the PLB (Figures 3g–3j). Besides, it is obvious that compared to CCs in subbasins, NSEs between the long-term TWSA (especially Li21) and the in-situ TWSA are very poor and negative in most scenarios, which may reveal that the long-term TWSAs from statistical models and hydrological models do not predict the in-situ measurements well. In Figures 3l–3o, WGHM shows the lowest RMSE in the DLB, the HRB, and the PLB, and HG19 has the smallest RMSE in the MRB.

These results suggest that HG19 and WGHM have significant dominance in the MLYRB and its four subbasins in test I, which reveals that the annual HG19 and the annual WGHM agree well with the in-situ TWSA.

4.1.2. Test II: Evaluation Using the Water Balance Equation

The overall performance statistics of the long-term TWSCs are calculated in the MLYRB and its three subbasins (i.e., DLB, HRB, and PLB) using the water balance equation from 2000 to 2016 (Figure 4). The statistical results clearly show that HG19C has a very significant dominance in various metrics of the MLYRB. HG19C depicts the highest CC (0.87) and NSE (0.74) in the MLYRB, with medians of CCs 2~14% and NSEs 1~23% higher than the other three long-term TWSC (i.e., Li21C, Liu21C, and WGHMC). Additionally, HG19C also has the smallest median of RMSE (13.29) among the long-term TWSCs. In three subbasins, HG19C demonstrates the best performance with the highest medians of CC and NSE and the lowest RMSE among the four long-term TWSC products, followed by Li21C, Liu21C, and WGHMC.

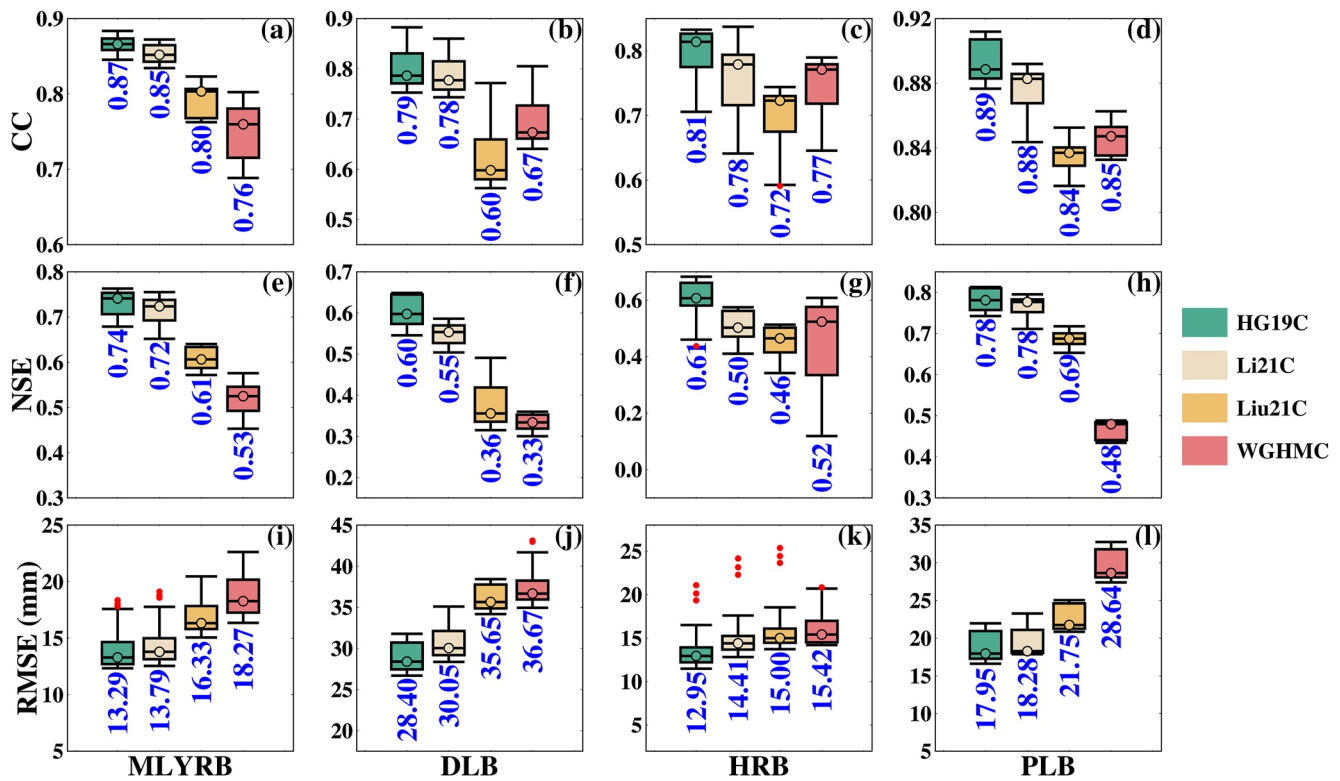


Figure 4. Boxplot of Correlation coefficient (CC), Nash-Sutcliffe efficiency (NSE), and root mean square error (RMSE) between the long-term terrestrial water storage change (TWSC) and 15 TWSCs from the water balance equation from 2000 to 2016 in the Middle-Lower reaches of the Yangtze River basin (MLYRB) and its three subbasins. The labeled red dots mean outliers, and the medians are marked in blue. (a–d) The CC in the MLYRB and subbasins, (e–h) the NSE in the MLYRB and subbasins, and (i–l) the RMSE in the MLYRB and subbasins.

4.1.3. Discussion of the Evaluation Results

To sum up, HG19 has the best comprehensive performance in the two groups of tests, so we select HG19 as the long-term TWSA and will conduct a time-frequency correlation analysis with ENSO in the follow-up. Meanwhile, it is necessary to discuss why HG19 performs better than other long-term TWSA (i.e., Li21, Liu21, and WGHM).

1. WGHM.

As the only long-term TWSA from the global hydrological model in this study, WGHM's performance is analyzed first. As described in Müller Schmied et al. (2021), WGHM has been calibrated to match observed long-term average annual water flux (e.g., streamflow) and water storage in all grid cells within the basin, which explains why the annual WGHM shows quite good agreement with the annual in-situ TWSA in test I. However, the monthly variations of WGHM have not been calibrated by the built-in programs, which leads to WGHM's poor performance in test II (Döll et al., 2020).

2. HG19, Li21, and Liu21.

Three long-term TWSA data sets generated by statistical models and inputted by GRACE and hydrometeorological data have different performances in two groups of tests. Generally, HG19 performs better than Li21 and Liu21, which could be explained from two perspectives.

First, the selection of the driven GRACE data is a potential reason. Referring to Liu et al. (2021), the reconstructed TWSA is strongly dependent on the driven GRACE data sets. Considering that HG19 is driven by JPLM, and Li21 and Liu21 are driven by CSRMs, we assess the performance of JPLM and CSRMs in the MLYRB and its subbasins using the evaluation framework in Section 3.6 (Figures S2 and S3 in Supporting Information S1). As shown in Figure S2 in Supporting Information S1, though CSRMs has higher CCs in the MLYRB and the DLB, JPLM shows higher CCs in the HRB, the MRB, and the PLB. Besides, JPLM has better performance in NSE and RMSE in the MLYRB and its subbasins. In Figure S3 in Supporting Information S1, we find that in the MLYRB and the HRB, JPLM performs better than CSRMs, while in the MRB and

the PLB, the performance of CSRM is superior. It can be concluded that JPLM has a better comprehensive performance in the evaluation programs, which leads to better performance of HG19 than Li21 and Liu21. Second, the difference in reconstruction algorithms is the direct reason. HG19 decompose TWSA as four items: a liner trend, an interannual component, a seasonal component, and a high-frequency sub-seasonal component, and then only reconstructs the nonseasonal variations (detrended and deseasonalized term) using a statistical model and then calibrate them at a monthly scale against the detrended and deseasonalized GRACE TWSA using a linear equation. Not only that but Humphrey and Gudmundsson (2019a) have regarded GRACE seasonal cycles as HG19's seasonal component. Therefore, HG19 is very close to GRACE mascons. F. Li et al. (2021) divided GRACE TWSA into spatial patterns, and temporal modes, then reconstructed the temporal modes using climate fields based on a statistical model, and finally combined the reconstructed temporal modes with GRACE TWSA spatial patterns to obtain Li21. However, F. Li et al. (2021) discarded temporal modes with low variance contribution of GRACE when establishing statistical models, which may lead to underestimating the low-frequency component, especially the interannual item. Liu21 is reconstructed directly from GRACE TWSA and climatic data sets without decomposing GRACE TWSA as many components. Since there are no more constraints on each component (e.g., detrended and deseasonalized term), the method in Liu et al. (2021) presumably lead to many uncertainties and ultimately lead to Liu21's poor performance.

4.2. Time-Domain Correlation Between the Long-Term TWSA and ENSO Indices in the MLYRB

Considering that ENSO shows 2–7 years of periodic characteristics of low frequency, a 13-month smoothing filter is utilized to suppress the high-frequency noise in both detrended and deseasonalized HG21 and ENSO indices to obtain more reliable results in the correlation test (Jin et al., 2020).

4.2.1. Uncertainty of CC Between the Long-Term TWSA and ENSO Indices

After selecting HG19 in Section 4.1, we add uncertainty analysis in this section that uses a Monte-Carlo simulation (Tiwari et al., 2009) to generate a distribution of CC. The calculation method is as follows:

1. At each month, we calculate the standard deviation of four long-term TWSAs and regard it as a measurement error.
2. We assume HG19 is Gaussian distribution with a standard deviation equal to our measurement error, and simulate many random instances (i.e., 10,000 in this study) of data sets from that distribution.
3. We remove the linear trend and the seasonal component from each data set and suppress its high-frequency residual using a 13-month moving average filter, and then calculate the CC for it and the 13-month moving average ENSO index.
4. We generate a distribution in the CCs from step 3 and take their mean value as the final CC.

In this study, the Monte-Carlo simulation enables us to quantify the uncertainty in the CC between the long-term TWSA and ENSO indices, which is much more informative than having a single value without a sense of uncertainty.

4.2.2. Correlations at Basin Scale

Correlations of HG19 and two ENSO indices in the MLYRB are shown in Figure 5 and Figure S4 in Supporting Information S1. Results demonstrate that CPI fails the significance test with $p < 0.05$, and the peak CC is only 0.14 with a 6-month time lag, while EPI (CC = 0.56, time lag = 6 months) pass the significant test. The lagged monthly EPI has good agreement with HG19 most of the time, especially during three strong El Niño years in 1983, 1998, and 2016 (mentioned in <https://ggweather.com/enso/oni.htm>), which revealed the Eastern pacific type ENSO's significant impacts on three extreme floodings in the MLYRB (Bett et al., 2018; Yuan et al., 2017). However, consistency between lagged CPI and HG19 is poor from 1979 to 2019, except for some periods, such as 2009–2011, in which the strong La Niña event starting in early 2010 was reported as one of the critical drivers of the once-in-a-50-year drought in middle 2011 preceded by six consecutive months of low precipitation from September 2010 (E. Lu et al., 2014; S. Yang et al., 2013).

Abnormal variations at 95% confidence are found in the detrended and deseasonalized TWSA during these four water extremes happened in 1983, 1998, 2011, and 2016, which show significant overwhelm surpluses in strong El Niño years (i.e., 1983, 1998, 2016) and deficit signals in strong La Niña year (2011) of TWSA in the MLYRB.

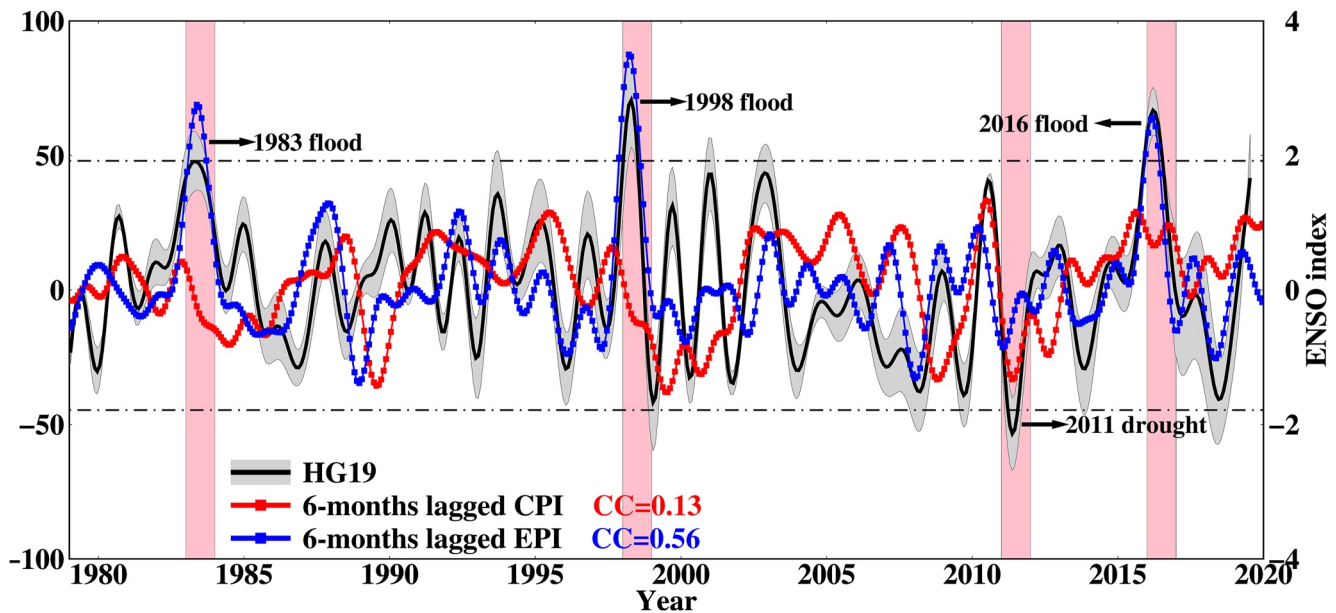


Figure 5. Correlation relationship of detrended and deseasonalized HG19 and two lagged El Niño-Southern Oscillation (ENSO) indices in the Middle-Lower reaches of the Yangtze River basin (MLYRB). Four water extremes to hit the MLYRB from 1979 to 2019 are labeled. Black dotted lines indicate the 95% confidence level. Pink rectangles reveal four strong El Niño and La Niña years that impact the MLYRB extremely (i.e., 1983, 1998, 2011, and 2016). The gray area depicts the standard deviation of HG19.

Interestingly, not all strong La Niña years after 1979 (i.e., 1989, 1999, 2000, and 2008, mentioned in <https://ggweather.com/enso/oni.htm>) accompany by significant anomalies in the detrended and deseasonalized TWSA. We attempt to explain this issue in two ways. First, some strong La Niña events have limited influence on TWSA in the MLYRB. Miralles et al. (2014) found a decrease in the amount of precipitation, evapotranspiration, and soil moisture in eastern and central Australia, southern Africa, and eastern South America, but not significant in the MLYRB during two strong La Niña events in 1989, 1999, and 2000. Second, compensation for TWSA from snowfalls or/and icy rainfalls. The 2008 La Niña is reported to be an essential driver of the heaviest snow disaster in southern China (including the MLYRB) from January to February 2008, costing 150 billion CNY and affecting 10 million people (Hui, 2009). However, during the 2008 La Niña episodes, compensation from snowfalls or/and icy rainfalls limited the reduction of TWSA. It is unlike the persistent lack of rainfall during the 2011 La Niña (Chen & Sun, 2010).

4.2.3. Correlations at Subbasin Scale

As shown in Figure 6, different subbasins respond differently to four water extremes. Among them, detrended and deseasonalized TWSA in the HRB is quite different from other subbasins (Figure 6b) that do not show significant peaks and valleys in 1998, 2011, and 2016. Nevertheless, performances of detrended and deseasonalized TWSA in the DLB, the MRB, and the PLB are similar to the MLYRB in these four strong El Niño and La Niña years with peaks and valleys. However, time nodes of peak values in the MRB appear 2–7 months later than those in the DLB and the PLB, while the time node of valley value is almost the same in these three subbasins (May or June 2011). It is obvious that when three El Niño extremes happen, the DLB and the PLB were affected first, and the MRB was affected several months later, which relates to the track of water vapor under the influence of El Niño (Yu et al., 2019; Zhai et al., 2016). However, the severe drought due to the 2011 La Niña almost simultaneously occurs in the MLYRB except in the HRB (E. Lu et al., 2014).

4.2.4. Correlations at Grid Cell Scale

There is a spatial variability in detrended and deseasonalized HG19's response for ENSO events in the MLYRB shown in Figure 7. Results suggest that over 52% of grid cells in the MLYRB failed the $p < 0.05$ significance test with CPI (Figures 7a and 7d and Table 2), while the passed cells are mainly distributed in the southern DLB and the HRB with the mean CC at only 0.20 and the mean time lag at 7.35 months. However, as shown in Figures 7b and 7e, about 56% of the grid cells that are mainly distributed in the DLB and the PLB passed the significance

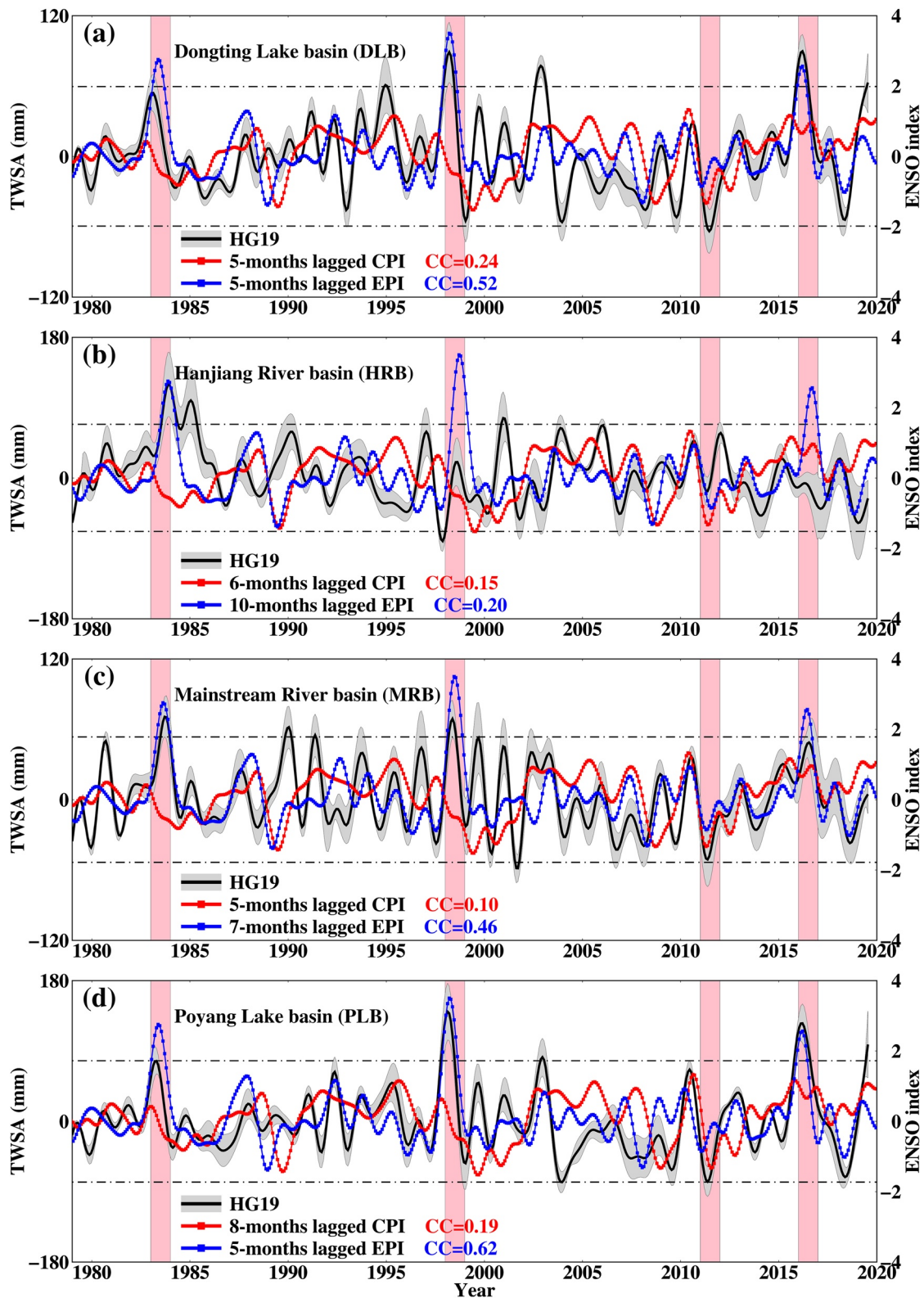


Figure 6. Correlation relationship between detrended and deseasonalized HG19 and two lagged El Niño-Southern Oscillation (ENSO) indices in four subbasins of the Middle-Lower reaches of the Yangtze River basin (MLYRB). (a) The Dongting Lake basin; (b) the Hanjiang River basin; (c) the Mainstream River basin; and (d) the Poyang Lake basin. Black dotted lines indicate the 95% confidence level. Pink rectangles reveal four strong El Niño and La Niña years that impact the MLYRB extremely (i.e., 1983, 1998, 2011, and 2016). The gray area depicts the standard deviation of HG19. CCs and time lags are referring to Table S2 in Supporting Information S1.

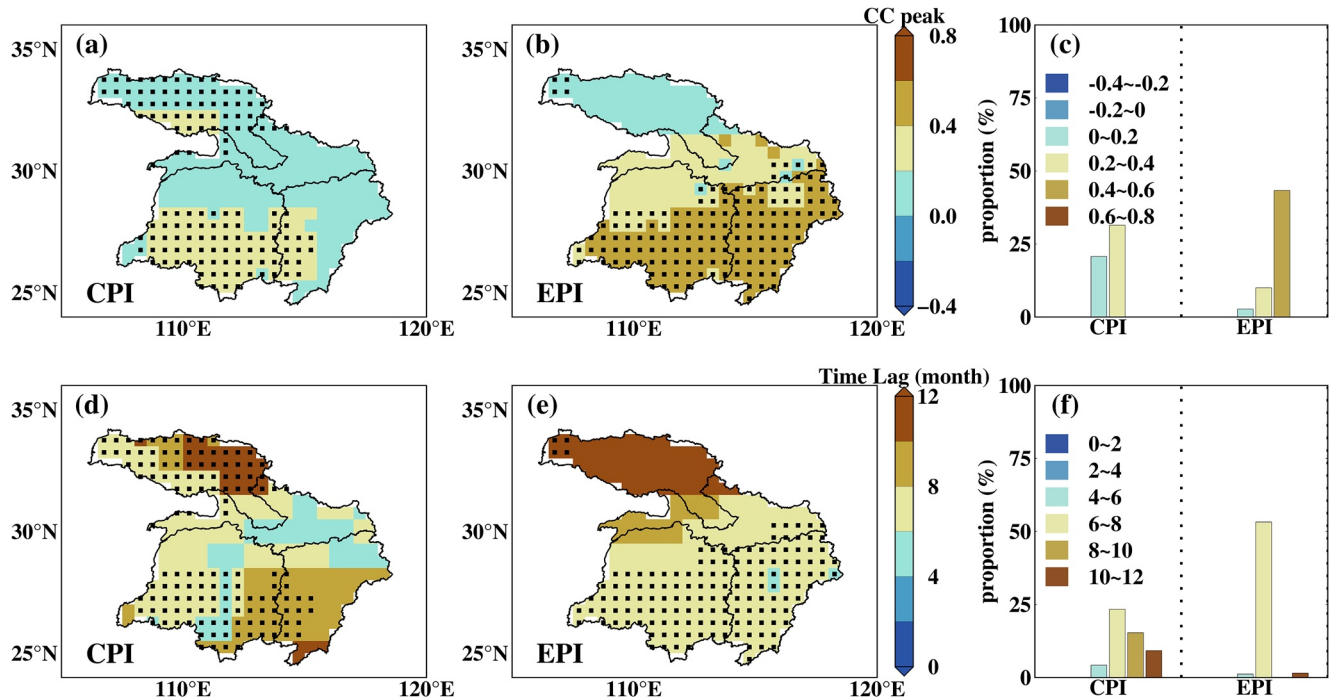


Figure 7. Correlation relationship of detrended and deseasonalized HG19 and two El Niño-Southern Oscillation (ENSO) indices at the grid scale. (a, b) The spatial distribution of Correlation coefficient (CC) peak values within the Middle-Lower reaches of the Yangtze River basin (MLYRB) in a $0.5^\circ \times 0.5^\circ$ grid cell between HG19 and two ENSO indices; (c) the histograms show the percent area that pass the $p < 0.05$ significant test between terrestrial water storage anomaly (TWSA) and ENSO indices with a different range of CC values; (d, e) the spatial distribution of time lags within the MLYRB between HG19 and two ENSO indices; (f) the histograms show the percent area that pass the $p < 0.05$ significant test between TWSA and ENSO indices with a different range of time lags. The black square in a grid cell indicates that the HG19 of this grid cell has passed the $p < 0.05$ significant test with ENSO indices.

test between EPI and HG19 with the mean CC of 0.47 at a typical time lag of 4–8 months, which is consistent with the series results.

Overall, among the two ENSO indices, CPI has a weaker link with HG19 than EPI. EPI not only shows a larger correlation coefficient (CC = 0.56), but also has a higher consistency with HG19 from 1979 to 2019 at multi-spatial scales, especially three strong El Niño years in 1983, 1998, and 2016. However, in the strong La Niña year 2011, CPI shows a higher correlation with TWSA than EPI.

4.3. Frequency-Domain Correlation Between the Long-Term TWSA and ENSO Indices in the MLYRB

As demonstrated in Figures 8a and 8f, resonance periodicities of HG19 and lagged ENSO indices (see Table S2 in Supporting Information S1) show that both CPI and EPI indices are all strongly correlated with HG19 at the 2–8 years band. CPI demonstrates significant positive correlations with HG19 from the late 2000s to the early 2010s at the 5–6 years band, and the $-\frac{1}{4}\pi$ phase angle manifests HG19 led CPI by $\frac{1}{8}$ period length. Therefore, CPI significantly impacts the fluctuation of HG19 from 2011 to the middle 2010s, which could explain the consistency of HG19 and CPI series during this period in Figure 5. In contrast, the extended period and darker red reveal a higher correlation between the long-term TWSA and EPI than CPI. The in-phase relationship with phase angle ranged $0 \sim \frac{1}{4}\pi$ from the middle 1980s to the late 1980s, demonstrating the phase of EPI is $0 \sim \frac{1}{8}$ period length lead by HG19, along with their significant positive correlation. Meanwhile, the rightward arrows during the late 2000s to the middle 2010s at the 2–8 years band reveal the in-phase correlation between HG19 and EPI with almost no time delay.

WTC results shown in Figures 8b–8e and 8g–8j reveal that the frequency correlation between HG19 and lagged ENSO indices in different subbasins is quite different. Right-downward arrows with phase angle about $-\frac{1}{4}\pi$ during the early and middle 2010s in Figure 8e suggest a pattern of HG19 leads that of CPI by $\frac{1}{8}$ period length in the PLB. Except the above, the coherence between HG19 of subbasins and CPI is relatively weak and

Table 2
The Proportion of the Number of Grid Points in Different CC Peak or Time Lag Value Ranges to the Total Number and the Mean Value

	HG19—CPI		HG19—EPI	
	Proportion (%)	Mean value	Proportion (%)	Mean value
CC peak ranges				
(−0.4~−0.2)	0	/	0	/
(−0.2~0)	0	/	0	/
(0~0.2)	20.69	0.14	2.68	0.16
(0.2~0.4)	31.42	0.24	9.96	0.31
(0.4~0.6)	0	/	43.30	0.50
(0.6~0.8)	0	/	0	/
Time lag ranges (month)				
(0~2)	0	/	0	/
(2~4)	0	/	0	/
(4~6)	4.21	5.00	1.15	5.00
(6~8)	23.37	6.07	53.26	6.10
(8~10)	15.33	8.35	0	/
(10~12)	9.20	10.00	1.53	10.10

Note. Results indicates statistical information in Figure 7 between HG19 and ENSO indices. Grid cells with TWSAs fail the $p < 0.05$ significant test with ENSO indices are not considered.

even shows a negative value in the HRB during the middle to late 1990s at the 2–3 years band, that reveals their significant negative correlation. However, the EPI shows a more vital link with HG19 in the frequency domain. In-phase correlations between HG19 in four subbasins and EPI are observed during the early 2000s to middle 2010s (2–8 years band) when phase angle remained within the range $0 \sim \frac{1}{4}\pi$, that reveals the about $\frac{1}{8}$ period length phase difference of them. In addition, the positive relationship during the early and late 1990s at 2–5 years band in Figure 8j represents EPI's significant impact on the long-term TWSA in the PLB during this period.

Generally, the EPI has significantly higher and positive coherence with HG19 in all subbasins than the CPI, which is the same as the series comparison results.

4.4. Causes of the Different Patterns in the Hanjiang River Basin and the Mainstream River Basin

According to time-frequency domain results in Sections 4.2 and 4.3, HG19 in the HRB and the MRB shows a weak correlation with both CPI and EPI. As suggested in Figures 7a and 7b, though about 87% of grid cells in the HRB pass the significant correlation test between HG19 and CPI, the mean CC peak and time lag are calculated as 0.03 and 6.75 months. Besides, although HG19 in the MRB has similar performance in the frequency domain to the DLB and the PLB, detrended and deseasonalized TWSA of only 20% and 17.78% grids in the MRB pass $p < 0.05$ significant test with CPI and EPI in the time domain, accompanied by the mean CC peaks at −0.01 and 0.52, and the mean time lags at 6.89 and 6.38, respectively. The causes of this different pattern of TWSA's response to ENSO in the HRB and the MRB need to be studied deeply.

Many studies reveal that TWSA in the HRB and the MRB is affected by two key drivers: climate change and human activity (Felfelani et al., 2017; Wang et al., 2022; Williams et al., 2022). In this study, the precipitation data set from CRU TS 4.06 and the human water use data set from PCR-GLOBWB 2.0 are utilized to assess the impact of climate change and artificial activities on TWSA variations in the HRB and the MRB. The goal is, first, to examine the influence of these two drivers on the TWSA in the past 20 years. If the effect is non-negligible, then second, whether this factor is significantly affected by ENSO. As a result, ideally, one or all of these two factors have significant effects on TWSA in the HRB and the MRB and are not significantly correlated with ENSO, thus explaining the poor correlation between TWSA and ENSO in these two basins.

4.4.1. Impact of Natural Factor

Precipitation is reported as a crucial path of ENSO affecting land water, especially in the Yangtze River basin (Sun et al., 2018; T. Zhang et al., 2019). Results shown in Figures 9a and 9b reveal that the detrended and deseasonalized HG19 of the HRB and the MRB display matches with the detrended and deseasonalized precipitation both monthly (CC = 0.78, time lag = 2 months, see Figure 9a) and seasonally (CC = 0.97, time lag = 2 months, see Figure 7b). However, as illustrated in Figures 9c and 9e, there is no significant correlation between precipitation and CPI, with mean CC at 0.06 and mean time lag at 7.99 months. In addition, Figures 9d and 9f show that only about 13% of grid cells, mainly distributed in the MRB, pass the significant test between precipitation and EPI with the mean CC at 0.31 and the mean time lag at 6.78 months.

As a result, the weak correlation between precipitation and ENSO indices in the HRB and the MRB could account for the mismatch between HG19 and ENSO indices from the perspective of the natural driver. However, the discussion about why ENSO has a weak link with precipitation in the HRB and the MRB is beyond the scope of the present study.

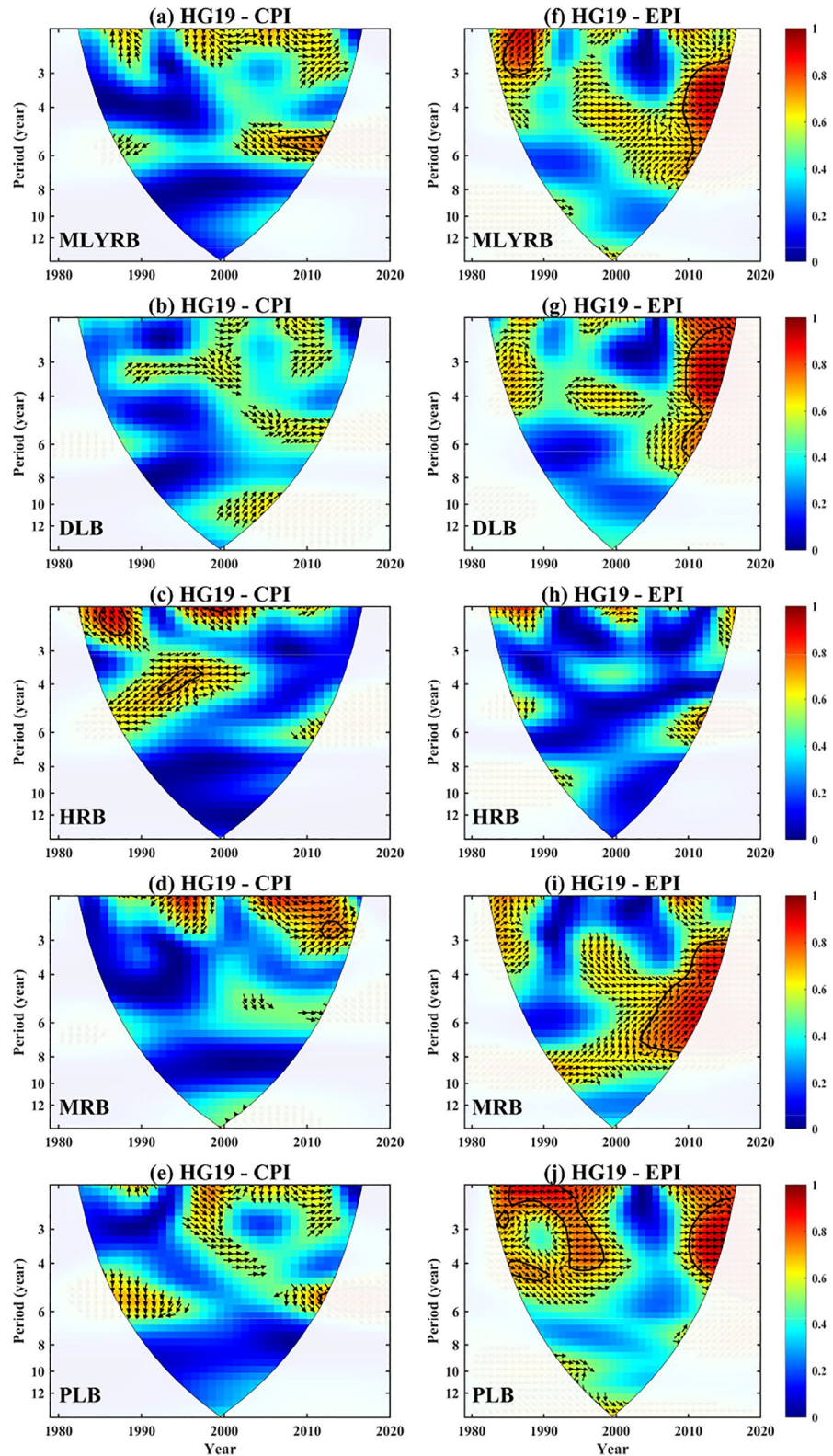


Figure 8. Wavelet coherence (WTC) of HG19 and two El Niño-Southern Oscillation (ENSO) indices in the Middle-Lower reaches of the Yangtze River basin (MLYRB) and four subbasins. (a–e) The WTC results between HG19 and CPI in these five basins; (f–j) the WTC results between HG19 and EPI in five basins. The opaque regions indicate no significant periodicities at the 95% confidence level. Leftward or rightward represent the in-phase or anti-phase relationship between two series, while downward or upward arrows represent HG19 lagged or led ENSO indices by 90° , respectively.

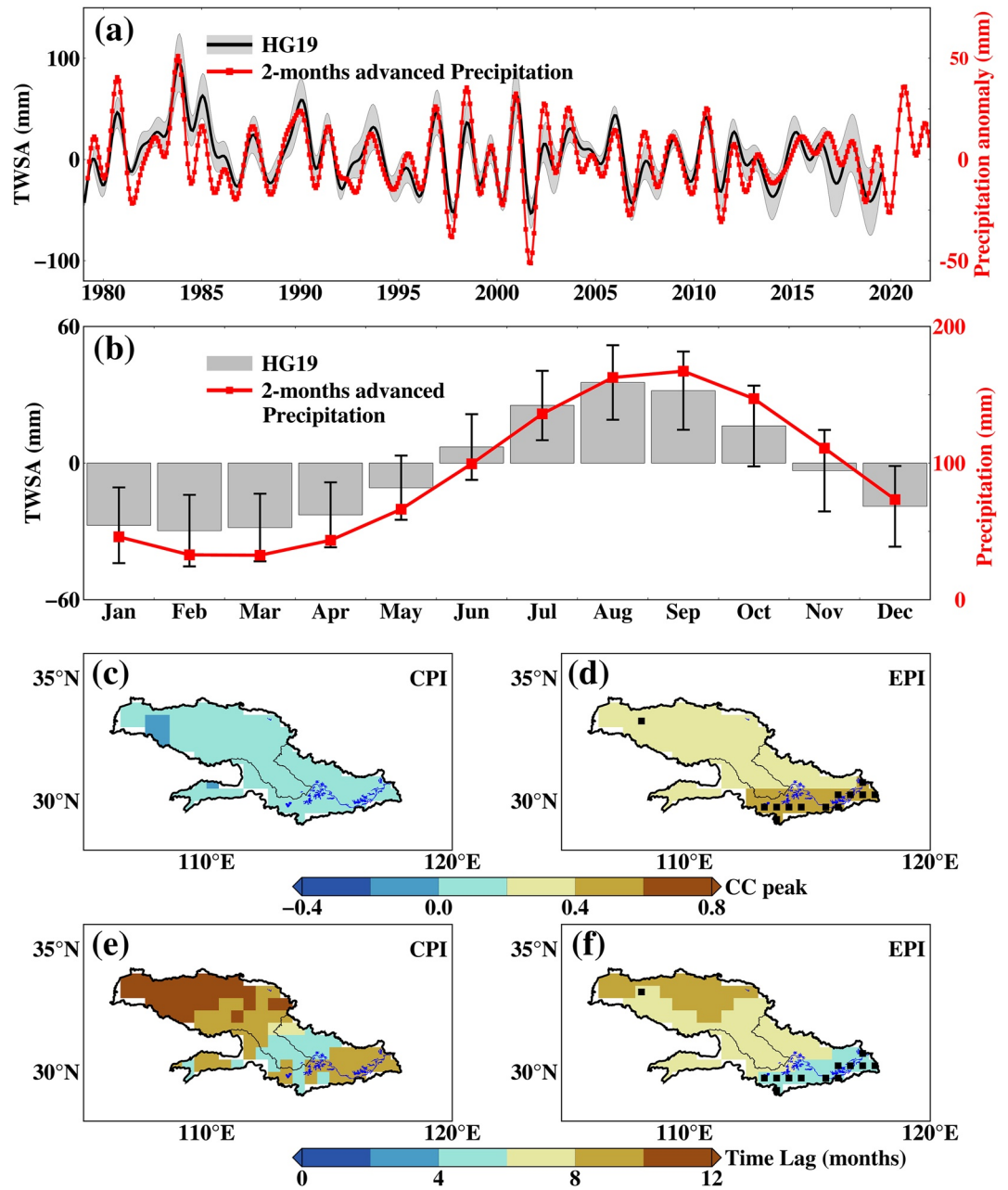


Figure 9. Comparison of HG19 and precipitation and correlation relationship between El Niño-Southern Oscillation (ENSO) indices and precipitation within the Hanjiang River basin (HRB) and the Mainstream River basin. (a) The series comparison between monthly HG19 and precipitation. The gray area depicts the standard deviation of HG19; (b) the mean seasonal cycles of the average of HG19 and precipitation; (c, d) the spatial distribution of Correlation coefficient peak values within the HRB and the MRB in a $0.5^\circ \times 0.5^\circ$ grid cell between precipitation and two ENSO indices; (e, f) the spatial distribution of time lags within the HRB and the MRB between precipitation and two ENSO indices. The black square in a grid cell indicates that the HG19 of this grid cell has passed the $p < 0.05$ significant test with ENSO indices.

4.4.2. Impact of Anthropogenic Factor

As shown in Figures 10a and 10b, we compare monthly HG19 and four monthly human water use outputs (i.e., human water use: industry, domestic, livestock, and irrigation water use) from 1979 to 2015. Note that the 2004 to 2009 averages have been removed from the human water use series for consistency with GRACE mascon. The annual amplitude of irrigation water use is much larger than those of the other three human water use items, which could also be proven by statistical results in Table 3 calculated by Equation 7 using the least square method.

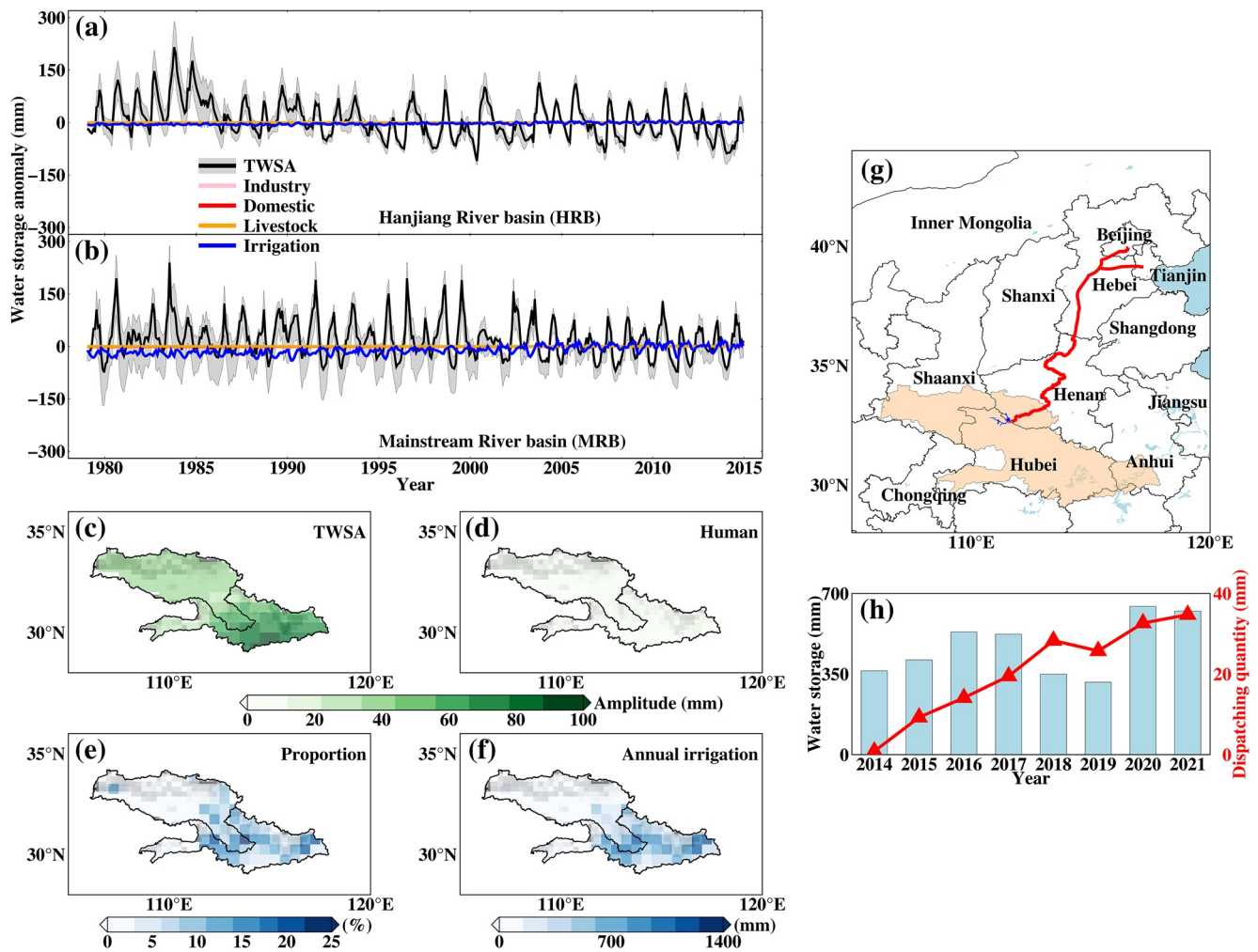


Figure 10. Impact of human activities on terrestrial water storage anomaly (TWSA) in the Hanjiang River basin (HRB) and the Mainstream River basin (MRB). (a, b) Series comparison of TWSA from HG19 and human water use from PCRaster Global Water Balance hydrological model 2.0 from 1979 to 2015. The gray area depicts the standard deviation of HG19; (c, d) the spatial distributions of annual amplitudes of TWSA and human water use at a $0.5^{\circ} \times 0.5^{\circ}$ grid cell from 1979 to 2015; (e) the percentage of the annual amplitude of human water use to the annual amplitude of TWSA; (f) the mean annual irrigation water uses from 1979 to 2015. (g) Tracks of the Central Route of the South-to-North Water Diversion Project (SNWD) (red lines); (h) the series comparison of yearly TWSA and SNWD from 2014 to 2021 from CWRC.

Among them, the MRB's annual amplitude of irrigation water use is about 5.8 times that of the HRB. It is due to a large number of plains (part of the Middle-Lower Yangtze Plain in China) distributed in the MRB and the great demand for irrigation water for paddy that ripens a year (Hu et al., 2013; Tian et al., 2021). However, the amplitudes of human water use are only small fractions of the amplitude of TWSA at about 4% and 16% in the HRB and the MRB, respectively, which reveals the limited impact of human activities in regional water storage.

The gridded annual amplitude of TWSA and human water use is shown in Figures 10c and 10d. We find that the amplitude of human water use is far smaller than that of TWSA, and their ratios have obvious spatial patterns (Figure 10e). The mean proportion is calculated as 6%, and proportions in the lower HRB and the Central MRB are much larger than that of other regions. Interestingly, regions with large proportions in Figure 10e are highly coincident with the distribution of the annual irrigation water uses in Figure 10f. It can be concluded that the TWSA of regions with higher-intensity irrigation is more vulnerable to anthropic activities in the HRB and the MRB. However, this impact is insignificant (Liu et al., 2021).

Inter-basin water diversion is the most direct way humans affect regional TWSA. As the largest inter-basin water diversion project in China, the SNWD is reported as an essential factor in the groundwater storage change of the North China Plain (Long et al., 2020), runoff of the Danjiangkou reservoir (L. Li et al., 2015), regional

Table 3

Statistical Results of Monthly TWSA From HG19 and Monthly Human Water Use From PCR-GLOBWB 2.0 in the HRB and the MRB From 1979 to 2015

Basin	Water storage	Amplitude (mm)	
		Annual	Semi-annual
Hanjiang River basin (HRB)	TWSA	40.88	12.24
	Industry water use	0.00	0.00
	Domestic water use	0.07	0.01
	Livestock water use	0.01	0.00
	Irrigation water use	1.41	1.35
	Human water use	1.49	1.36
Mainstream River basin (MRB)	TWSA	54.05	11.65
	Industry water use	0.01	0.00
	Domestic water use	0.09	0.01
	Livestock water use	0.01	0.00
	Irrigation water use	8.54	2.69
	Human water use	8.65	2.70

Note. Human water use is the sum of industry, domestic, livestock, and irrigation water use. Annual and semi-annual amplitudes are calculated by Equation 7 using the least square method.

environmental response (Lin et al., 2012), and so on. In this study, we take SNWD as an example to evaluate the impact of inter-basin water diversion on TWSA in the HRB. Results in Figure 10 indicate that although the cumulative amount of water diversion is enormous, the average annual water diversion volume of SNWD is about 20.65 mm, which is only 4.39% of the water storage of the HRB and the MRB (470.45 mm). It can be seen that impact of SNWD on TWS in the HRB and the MRB is extremely limited.

Combining results from Figures 9 to 10, one of the main reasons for the mismatch between TWSA and the ENSO index in the HRB and the MRB is the feeble impact of ENSO on precipitation. However, because of the human activity's insignificant impact on TWSA, this mismatch is unrelated to human activities, including the SNWD, China's largest inter-basin water diversion project.

This study provides an example for subsequent relevant studies focusing on long-term water storage in the MLYRB. In addition, conclusions related to natural and anthropic factors provide suitable guidance for optimizing regional water resources management.

It should be noted that there are some limitations in this study. First, though we have developed an evaluation framework using two groups of tests, the time periods of the two tests are different, which probably leads to different evaluation results between the two tests. For example, WGHM has a quite good performance in test I, but a poor performance in test II. We hope that in the future, CWRC will be able to release water storage products in the MLYRB with longer time spans. Second, in Section 4.4, we regard precipitation as the only natural factor. Though precipitation is proven as the most important natural factor in water storage variations in the MLYRB, it is not the only one (T. Zhang et al., 2019). As a result, we will consider other natural factors in the follow-up studies, including temperature, sunshine duration, and wind speed.

5. Conclusions

Under rapid industrialization and urbanization and the ensuing anthropogenic global warming, climate change hazards closely related to the ENSO events have been frequent extreme water events in the MLYRB over the centuries. With the support of TWSA monitored by GRACE and GRACE-FO missions, these extreme events can be detected directly. However, the too short period (2002 to the present) of GRACE and GRACE-FO limits robustness to the assessment of ENSO's impact on TWSA and need to be extended. In addition, regional variations of TWSA's response to ENSO caused by the difference in climatic conditions and human activity intensity

in the MLYRB need to be confirmed. To solve these two questions, we assess four long-term TWSA data sets in the MLYRB using an evaluation framework and then choose the best one. Further, we explore the driving effect of ENSO on long-term TWSA in the time-frequency domain at the basin, subbasin, and grid cell scales, respectively. Finally, in view of the spatial-variable patterns of ENSO's impact on TWSA, we attempted to explain in detail from natural and man-made perspectives.

Results indicates that HG19 has the best all-around performance in the evaluation tests, so it is regarded as the long-term TWSA making further analysis. Both time and frequency domain results show that the EPI (CC = 0.56, time lag = 6 months, $p < 0.05$) has a higher correlation with HG19 than the CPI (CC = 0.14, time lag = 6 months, $p > 0.05$) in the MLYRB, and the same in two of the four subbasins (the DLB and the PLB). However, TWSA in the other two subbasins (the HRB and the MRB) demonstrates poor correlations with the CPI and EPI.

To explain the different regimes in the HRB and the MRB, precipitation from CRU and artificial activity data sets from PCR-GLOBWB model are utilized to evaluate the impact of natural and human factors on TWSA. We find that precipitation is the one of the key drivers of TWSA in the HRB and MRB (CC = 0.81, time lag = 2 months). Further analysis indicates that ENSO has almost no link with precipitation in the HRB and MRB. However, the annual amplitude of human activities is calculated as only 6% of that of TWSA. As a result, this diverse pattern in the HRB and the MRB could be explained as the weak impact of ENSO on precipitation, but artificial activities' (including inter-basin water diversion) impact on regional TWSA is limited.

Overall, this study reflects the multi-spatial scale response characteristics of the long-term TWSA to ENSO in the time-frequency domain in the MLYRB and helps to promote appropriate use of water resources operations and climate change responses and highlight areas for future improvements.

Conflict of Interest

The authors declare no conflicts of interest relevant to this study.

Data Availability Statement

The data used in this study are publicly available. The CSR and JPL RL06 GRACE time-varying gravity field mascon models are downloaded from <http://www2.csr.utexas.edu/grace> and <https://grace.jpl.nasa.gov/data>. Long-term TWSA abbreviated as HG19, Li21, and WGHM can be obtained from https://figshare.com/articles/dataset/GRACE-REC_A_reconstruction_of_climate-driven_water_storage_changes_over_the_last_century/7670849 (Humphrey & Gudmundsson, 2019b), <https://datadryad.org/stash/dataset/doi:10.5061/dryad.z612jm6bt> (F. Li, 2021), and <https://zenodo.org/record/7419307#.ZFXEQuxBwWM> (Döll et al., 2014). Precipitation models of CRU TS 4.06, ERA5, GPCC v2022, and U.Delaware v501 are downloaded from <https://crudata.uea.ac.uk/cru/data/hrg/>, <https://doi.org/10.24381/cds.68d2bb30> (Muñoz Sabater, 2019), https://doi.org/10.5676/DWD_GPCC/FD_M_V2020_050 (Schneider et al., 2020), and https://psl.noaa.gov/data/gridded/data.UDeI_AirT_Precip.html. Evapotranspiration models of REA ET and GLEAM v3.3a are available from <https://doi.org/10.5281/zenodo.4595941> (J. Lu et al., 2021b) and <https://www.gleam.eu/>. Monthly discharge measurements, yearly water storage and yearly in-situ inter-basin water diversion measurements are available via Changjiang Water Resources Commission of the Ministry of Water Resources (CWRC, <http://www.cjw.gov.cn/>). Giving the CWRC website is in Chinese, we collated these above three data sets and uploaded them to <https://zenodo.org/record/7902225#.ZFYZuxBwWN> (Jin, 2023). Two type of ENSO indices are available from https://icar.nuist.edu.cn/_upload/article/files/bb/2a/313c21ce4b90bdc2bcd3ebb73dca/1ebebac6-bc54-45d1-8c7e-4a7c18426f0d.txt and https://icar.nuist.edu.cn/_upload/article/files/bb/2a/313c21ce4b90bdc2bcd3ebb73dca/6bae2475-6cd0-4bbb-adde-967cc084836c.txt. PCR-GLOBWB 2.0 model and input data are available in https://github.com/UU-Hydro/PCR-GLOBWB_model and <https://zenodo.org/record/1045339#.XWU7E2P5aR> (Sutanudjaja et al., 2017). The authors gratefully appreciate these publicly accessible data sets used in this research.

Processing of the data has been done using Matlab_R2021a (<https://ww2.mathworks.cn/products/matlab.html>), and the Generic Mapping Tool (GMT, <https://www.generic-mapping-tools.org/>) software is used for drawing figures.

Acknowledgments

This study is supported by the National Natural Science Foundation of China under Grant 42192534, the Natural Science Foundation of Hubei Province for Distinguished Young Scholars under Grant 2022CFA090, and the Special Fund of Hubei Luojia Laboratory under Grant 220100001.

References

- Andrews, E. D., Antweiler, R. C., Neiman, P. J., & Ralph, F. M. (2004). Influence of ENSO on flood frequency along the California Coast. *Journal of Climate*, 17(2), 337–348. [https://doi.org/10.1175/1520-0442\(2004\)017<0337:IOEOF>2.0.CO;2](https://doi.org/10.1175/1520-0442(2004)017<0337:IOEOF>2.0.CO;2)
- Ayantobo, O. O., Wei, J., & Wang, G. (2022). Climatology of landfalling atmospheric rivers and its attribution to extreme precipitation events over Yangtze River basin. *Atmospheric Research*, 270, 106077. <https://doi.org/10.1016/j.atmosres.2022.106077>
- Bett, P. E., Scaife, A. A., Li, C., Hewitt, C., Golding, N., Zhang, P., et al. (2018). Seasonal forecasts of the summer 2016 Yangtze River basin rainfall. *Advances in Atmospheric Sciences*, 35(8), 918–926. <https://doi.org/10.1007/s00376-018-7210-y>
- Boker, S. M., Rotondo, J. L., Xu, M., & King, K. (2002). Windowed cross-correlation and peak picking for the analysis of variability in the association between behavioral time series. *Psychological Methods*, 7(3), 338–355. <https://doi.org/10.1037/1082-989X.7.3.338>
- Chen, J., Cazenave, A., Dahle, C., Llovel, W., Panet, I., Pfeffer, J., & Moreira, L. (2022). Applications and challenges of GRACE and GRACE follow-on satellite gravimetry. *Surveys in Geophysics*, 43(1), 305–345. <https://doi.org/10.1007/s10712-021-09685-x>
- Chen, J., & Sun, L. (2010). Using MODIS EVI to detect vegetation damage caused by the 2008 ice and snow storms in south China. *Journal of Geophysical Research*, 115, G00H04. <https://doi.org/10.1029/2009JG001246>
- Chen, J., Tapley, B., Rodell, M., Seo, K., Wilson, C., Scanlon, B. R., & Pokhrel, Y. (2020). Basin-scale river runoff estimation from GRACE gravity satellites, climate models, and in situ observations: A case study in the Amazon basin. *Water Resources Research*, 56(10), e2020WR028032. <https://doi.org/10.1029/2020WR028032>
- Cheng, H., Wang, W., van Oel, P. R., Lu, J., Wang, G., & Wang, H. (2021). Impacts of different human activities on hydrological drought in the Huaihe River basin based on scenario comparison. *Journal of Hydrology: Regional Studies*, 37, 100909. <https://doi.org/10.1016/j.ejrh.2021.100909>
- Cobon, D. H., Ewai, M., Inape, K., & Bourke, R. M. (2016). Food shortages are associated with droughts, floods, frosts and ENSO in Papua New Guinea. *Agricultural Systems*, 145, 150–164. <https://doi.org/10.1016/j.agry.2016.02.012>
- De Boor, C. (1978). *A practical guide to splines* (Rev. ed.). Springer.
- Deng, S., Liu, Y., & Zhang, W. (2023). A comprehensive evaluation of GRACE-like Terrestrial Water Storage (TWS) reconstruction products at an interannual scale during 1981–2019. *Water Resources Research*, 59(3), e2022WR034381. <https://doi.org/10.1029/2022WR034381>
- Dilley, M., & Heyman, B. N. (1995). ENSO and disaster: Droughts, floods and El Niño/Southern Oscillation warm events. *Disasters*, 19(3), 181–193. <https://doi.org/10.1111/j.1467-7717.1995.tb00338.x>
- Döll, P., Kaspar, F., & Lehner, B. (2003). A global hydrological model for deriving water availability indicators: Model tuning and validation. *Journal of Hydrology*, 270(1–2), 105–134. [https://doi.org/10.1016/S0022-1694\(02\)00283-4](https://doi.org/10.1016/S0022-1694(02)00283-4)
- Döll, P., Müller Schmied, H., Schuh, C., Portmann, F. T., & Eicker, A. (2014). Data sources for the groundwater depletion manuscript in Water Resources Research (1.0) [Dataset]. Zenodo. <https://doi.org/10.5281/zenodo.7419307>
- Döll, P., Trautmann, T., Göllner, M., & Schmied, H. M. (2020). A global-scale analysis of water storage dynamics of inland wetlands: Quantifying the impacts of human water use and man-made reservoirs as well as the unavoidable and avoidable impacts of climate change. *Ecology*, 13(1), e2175. <https://doi.org/10.1002/eco.2175>
- Dottori, F., Szewczyk, W., Ciscar, J.-C., Zhao, F., Alfieri, L., Hirabayashi, Y., et al. (2018). Increased human and economic losses from river flooding with anthropogenic warming. *Nature Climate Change*, 8(9), 781–786. <https://doi.org/10.1038/s41558-018-0257-z>
- Emerton, R., Cloke, H. L., Stephens, E. M., Zsoter, E., Woolnough, S. J., & Pappenberger, F. (2017). Complex picture for likelihood of ENSO-driven flood hazard. *Nature Communications*, 8(1), 14796. <https://doi.org/10.1038/ncomms14796>
- Felfelani, F., Wada, Y., Longuevergne, L., & Pokhrel, Y. N. (2017). Natural and human-induced terrestrial water storage change: A global analysis using hydrological models and GRACE. *Journal of Hydrology*, 553, 105–118. <https://doi.org/10.1016/j.jhydrol.2017.07.048>
- Fu, C., Wu, H., Zhu, Z., Song, C., Xue, B., Wu, H., et al. (2021). Exploring the potential factors on the striking water level variation of the two largest semi-arid-region lakes in northeastern Asia. *CATENA*, 198, 105037. <https://doi.org/10.1016/j.catena.2020.105037>
- Grinsted, A., Moore, J. C., & Jevrejeva, S. (2004). Application of the cross wavelet transform and wavelet coherence to geophysical time series. *Nonlinear Processes in Geophysics*, 11(5/6), 561–566. <https://doi.org/10.5194/npg-11-561-2004>
- Hersbach, H., Bell, B., Berrisford, P., Hirahara, S., Horányi, A., Muñoz-Sabater, J., et al. (2020). The ERA5 global reanalysis. *Quarterly Journal of the Royal Meteorological Society*, 146(730), 1999–2049. <https://doi.org/10.1002/qj.3803>
- Hinkel, J., Lincke, D., Vafeidis, A. T., Perrette, M., Nicholls, R. J., Tol, R. S. J., et al. (2014). Coastal flood damage and adaptation costs under 21st century sea-level rise. *Proceedings of the National Academy of Sciences*, 111(9), 3292–3297. <https://doi.org/10.1073/pnas.1222469111>
- Hu, L., Chao, Z., Gu, M., Li, F., Chen, L., Liu, B., et al. (2013). Evidence for a Neolithic Age fire-irrigation paddy cultivation system in the lower Yangtze River Delta, China. *Journal of Archaeological Science*, 40(1), 72–78. <https://doi.org/10.1016/j.jas.2012.04.021>
- Hui, G. (2009). China's snow disaster in 2008, who is the principal player? *International Journal of Climatology*, 29(14), 2191–2196. <https://doi.org/10.1002/joc.1859>
- Humphrey, V., & Gudmundsson, L. (2019a). GRACE-REC: A reconstruction of climate-driven water storage changes over the last century. *Earth System Science Data*, 11(3), 1153–1170. <https://doi.org/10.5194/essd-11-1153-2019>
- Humphrey, V., & Gudmundsson, L. (2019b). GRACE-REC: A reconstruction of climate-driven water storage changes over the last century [Dataset]. figshare, 11(3), 1153–1170. <https://doi.org/10.6084/m9.figshare.7670849.v3>
- Humphrey, V., Gudmundsson, L., & Seneviratne, S. I. (2017). A global reconstruction of climate-driven subdecadal water storage variability. *Geophysical Research Letters*, 44(5), 2300–2309. <https://doi.org/10.1002/2017GL072564>
- IPCC. (2022). *Climate change 2022: Impacts, adaptation and vulnerability*. Cambridge University Press.
- Jammazi, R., & Aloui, C. (2015). Environment degradation, economic growth and energy consumption nexus: A wavelet-windowed cross correlation approach. *Physica A: Statistical Mechanics and Its Applications*, 436, 110–125. <https://doi.org/10.1016/j.physa.2015.05.058>
- Jiao, D., Wang, D., & Lv, H. (2020). Effects of human activities on hydrological drought patterns in the Yangtze River basin, China. *Natural Hazards*, 104(1), 1111–1124. <https://doi.org/10.1007/s11069-020-04206-2>
- Jin, T. (2023). Three datasets from the Changjiang Water Resources Commission of the Ministry of Water Resources [Dataset]. Zenodo. <https://doi.org/10.5281/zenodo.7902225>
- Jin, T., Li, X., Shum, C. K., Ding, H., & Xu, X. (2020). The balance and abnormal increase of global ocean mass change from land using GRACE. *Earth and Space Science*, 7(5), e2020EA001104. <https://doi.org/10.1029/2020EA001104>
- Kao, H.-Y., & Yu, J.-Y. (2009). Contrasting Eastern-Pacific and Central-Pacific types of ENSO. *Journal of Climate*, 22(3), 615–632. <https://doi.org/10.1175/2008JCLI2309.1>
- Kreibich, H., Van Loon, A. F., Schröter, K., Ward, P. J., Mazzoleni, M., Sairam, N., et al. (2022). The challenge of unprecedented floods and droughts in risk management. *Nature*, 608(7921), 80–86. <https://doi.org/10.1038/s41586-022-04917-5>

- Kug, J.-S., Jin, F.-F., & An, S.-I. (2009). Two types of El Niño Events: Cold tongue El Niño and warm pool El Niño. *Journal of Climate*, 22(6), 1499–1515. <https://doi.org/10.1175/2008JCLI2624.1>
- Li, F. (2021). Data from: Long-term (1979-present) total water storage anomalies over the global land derived by reconstructing GRACE data [Dataset]. Dryad. <https://doi.org/10.5061/dryad.z612jm6bt>
- Li, F., Kusche, J., Chao, N., Wang, Z., & Löcherer, A. (2021). Long-term (1979-present) total water storage anomalies over the global land derived by reconstructing GRACE data. *Geophysical Research Letters*, 48(8), e2021GL093492. <https://doi.org/10.1029/2021GL093492>
- Li, F., Kusche, J., Rietbroek, R., Wang, Z., Forootan, E., Schulze, K., & Lück, C. (2020). Comparison of data-driven techniques to reconstruct (1992–2002) and predict (2017–2018) GRACE-like gridded total water storage changes using climate inputs. *Water Resources Research*, 56(5), e2019WR026551. <https://doi.org/10.1029/2019WR026551>
- Li, L., Zhang, L., Xia, J., Gippel, C. J., Wang, R., & Zeng, S. (2015). Implications of modelled climate and land cover changes on runoff in the middle route of the south to north water transfer project in China. *Water Resources Management*, 29(8), 2563–2579. <https://doi.org/10.1007/s11269-015-0957-3>
- Lin, C., Suh, S., & Pfister, S. (2012). Does South-To-North Water transfer reduce the environmental impact of water consumption in China? *Journal of Industrial Ecology*, 16(4), 647–654. <https://doi.org/10.1111/j.1530-9290.2012.00500.x>
- Liu, B., Zou, X., Yi, S., Sneeuw, N., Cai, J., & Li, J. (2021). Identifying and separating climate- and human-driven water storage anomalies using GRACE satellite data. *Remote Sensing of Environment*, 263, 112559. <https://doi.org/10.1016/j.rse.2021.112559>
- Long, D., Chen, X., Scanlon, B. R., Wada, Y., Hong, Y., Singh, V. P., et al. (2016). Have GRACE satellites overestimated groundwater depletion in the Northwest India Aquifer? *Scientific Reports*, 6(1), 24398. <https://doi.org/10.1038/srep24398>
- Long, D., Pan, Y., Zhou, J., Chen, Y., Hou, X., Hong, Y., et al. (2017). Global analysis of spatiotemporal variability in merged total water storage changes using multiple GRACE products and global hydrological models. *Remote Sensing of Environment*, 192, 198–216. <https://doi.org/10.1016/j.rse.2017.02.011>
- Long, D., Yang, W., Scanlon, B. R., Zhao, J., Liu, D., Burek, P., et al. (2020). South-to-North Water Diversion stabilizing Beijing's groundwater levels. *Nature Communications*, 11(1), 3665. <https://doi.org/10.1038/s41467-020-17428-6>
- Lu, E., Cai, W., Jiang, Z., Zhang, Q., Zhang, C., Higgins, R. W., & Halpert, M. S. (2014). The day-to-day monitoring of the 2011 severe drought in China. *Climate Dynamics*, 43(1–2), 1–9. <https://doi.org/10.1007/s00382-013-1987-2>
- Lu, J., Wang, G., Chen, T., Li, S., Hagan, D. F. T., Kattel, G., et al. (2021a). A harmonized global land evaporation dataset from model-based products covering 1980–2017. *Earth System Science Data*, 13(12), 5879–5898. <https://doi.org/10.5194/essd-13-5879-2021>
- Lu, J., Wang, G., Chen, T., Li, S., Hagan, D. F. T., Kattel, G., et al. (2021b). A harmonized global land evaporation dataset from model-based products covering 1980–2017 [Dataset]. Zenodo, 13(12), 5879–5898. <https://doi.org/10.5281/zenodo.4595941>
- Maraun, D., & Kurths, J. (2004). Cross wavelet analysis: Significance testing and pitfalls. *Nonlinear Processes in Geophysics*, 11(4), 505–514. <https://doi.org/10.5194/npg-11-505-2004>
- Miralles, D. G., Holmes, T. R. H., De Jeu, R. A. M., Gash, J. H., Meesters, A. G. C. A., & Dolman, A. J. (2011). Global land-surface evaporation estimated from satellite-based observations. *Hydrology and Earth System Sciences*, 15(2), 453–469. <https://doi.org/10.5194/hess-15-453-2011>
- Miralles, D. G., van den Berg, M. J., Gash, J. H., Parinussa, R. M., de Jeu, R. A. M., Beck, H. E., et al. (2014). El Niño–La Niña cycle and recent trends in continental evaporation. *Nature Climate Change*, 4(2), 122–126. <https://doi.org/10.1038/nclimate2068>
- Müller Schmied, H., Cáceres, D., Eisner, S., Flörke, M., Herbert, C., Niemann, C., et al. (2021). The global water resources and use model WaterGAP v2.2d: Model description and evaluation. *Geoscientific Model Development*, 14(2), 1037–1079. <https://doi.org/10.5194/gmd-14-1037-2021>
- Muñoz Sabater, J. (2019). ERA5-land monthly averaged data from 1950 to present [Dataset]. Copernicus Climate Change Service (C3S) Climate Data Store (CDS). <https://doi.org/10.24381/cds.68d2bb30>
- New, M., Hulme, M., & Jones, P. (2000). Representing twentieth-century space–time climate variability. Part II: Development of 1901–96 monthly grids of terrestrial surface climate. *Journal of Climate*, 13(13), 2217–2238. [https://doi.org/10.1175/1520-0442\(2000\)013<2217:RTCSTC>2.0.CO;2](https://doi.org/10.1175/1520-0442(2000)013<2217:RTCSTC>2.0.CO;2)
- Pervez, M. S., & Henebry, G. M. (2015). Spatial and seasonal responses of precipitation in the Ganges and Brahmaputra river basins to ENSO and Indian Ocean dipole modes: Implications for flooding and drought. *Natural Hazards and Earth System Sciences*, 15(1), 147–162. <https://doi.org/10.5194/nhess-15-147-2015>
- Phillips, T., Nerem, R. S., Fox-Kemper, B., Famiglietti, J. S., & Rajagopalan, B. (2012). The influence of ENSO on global terrestrial water storage using GRACE. *Geophysical Research Letters*, 39(16), n/a. <https://doi.org/10.1029/2012GL052495>
- Qi, W., Feng, L., Yang, H., Liu, J., Zheng, Y., Shi, H., et al. (2022). Economic growth dominates rising potential flood risk in the Yangtze River and benefits of raising dikes from 1991 to 2015. *Environmental Research Letters*, 17(3), 034046. <https://doi.org/10.1088/1748-9326/ac5561>
- Räsänen, T. A., & Kumm, M. (2013). Spatiotemporal influences of ENSO on precipitation and flood pulse in the Mekong River basin. *Journal of Hydrology*, 476, 154–168. <https://doi.org/10.1016/j.jhydrol.2012.10.028>
- Reager, J. T., Gardner, A. S., Famiglietti, J. S., Wiese, D. N., Eicker, A., & Lo, M.-H. (2016). A decade of sea level rise slowed by climate-driven hydrology. *Science*, 351(6274), 699–703. <https://doi.org/10.1126/science.aad8386>
- Ren, D., Liu, L., Huang, L., & Zhou, L. (2022). Hydrological variability and loading deformation in the Yangtze River basin based on modern geodetic means. *All Earth*, 34(1), 66–80. <https://doi.org/10.1080/27669645.2022.2098895>
- Rezaei, A., & Gurdak, J. J. (2020). Large-scale climate variability controls on climate, vegetation coverage, lake and groundwater storage in the Lake Urmia watershed using SSA and wavelet analysis. *Science of the Total Environment*, 724, 138273. <https://doi.org/10.1016/j.scitotenv.2020.138273>
- Rodell, M., Famiglietti, J. S., Wiese, D. N., Reager, J. T., Beaudoin, H. K., Landerer, F. W., & Lo, M.-H. (2018). Emerging trends in global freshwater availability. *Nature*, 557(7707), 651–659. <https://doi.org/10.1038/s41586-018-0123-1>
- Save, H., Bettadpur, S., & Tapley, B. D. (2016). High-resolution CSR GRACE RL05 mascons. *Journal of Geophysical Research: Solid Earth*, 121(10), 7547–7569. <https://doi.org/10.1002/2016JB013007>
- Scanlon, B. R., Zhang, Z., Rateb, A., Sun, A., Wiese, D., Save, H., et al. (2019). Tracking seasonal fluctuations in land water storage using global models and GRACE satellites. *Geophysical Research Letters*, 46(10), 5254–5264. <https://doi.org/10.1029/2018GL081836>
- Scanlon, B. R., Zhang, Z., Save, H., Sun, A. Y., Müller Schmied, H., van Beek, L. P. H., et al. (2018). Global models underestimate large decadal declining and rising water storage trends relative to GRACE satellite data. *Proceedings of the National Academy of Sciences*, 115(6), E1080–E1089. <https://doi.org/10.1073/pnas.1704665115>
- Schneider, U., Becker, A., Finger, P., Rustemeier, E., & Ziese, M. (2020). GPCC full data monthly product version 2020 at 0.5°: Monthly land-surface precipitation from rain-gauges built on GTS-based and historical data [Dataset]. https://doi.org/10.5676/DWD_GPCC/FD_M_V2020_050

- Schneider, U., Hänsel, S., Finger, P., Rustemeier, E., & Ziese, M. (2022). GPCP full data monthly version 2022 at 0.5°: Monthly land-surface precipitation from rain-gauges built on GTS-based and historic data: Globally gridded monthly totals (Version 2022) [NetCDF]. Global Precipitation Climatology Centre (GPCC) at Deutscher Wetterdienst. https://doi.org/10.5676/DWD_GPCP/FD_M_V2022_050
- Su, L., Miao, C., Duan, Q., Lei, X., & Li, H. (2019). Multiple-wavelet coherence of world's large rivers with meteorological factors and ocean signals. *Journal of Geophysical Research: Atmospheres*, *124*(9), 4932–4954. <https://doi.org/10.1029/2018JD029842>
- Sullivan, A., Luo, J.-J., Hirst, A. C., Bi, D., Cai, W., & He, J. (2016). Robust contribution of decadal anomalies to the frequency of central-Pacific El Niño. *Scientific Reports*, *6*(1), 38540. <https://doi.org/10.1038/srep38540>
- Sun, Z., Zhu, X., Pan, Y., Zhang, J., & Liu, X. (2018). Drought evaluation using the GRACE terrestrial water storage deficit over the Yangtze River basin, China. *Science of the Total Environment*, *634*, 727–738. <https://doi.org/10.1016/j.scitotenv.2018.03.292>
- Sutanudjaja, E. H., van Beek, R., Wanders, N., Wada, Y., Bosmans, J. H. C., Drost, N., et al. (2017). PCR-GLOBWB 2 input files version 2017_11_beta_1 (v_2017_11_beta_1) [Dataset]. Zenodo. <https://doi.org/10.5281/zenodo.1045339>
- Sutanudjaja, E. H., van Beek, R., Wanders, N., Wada, Y., Bosmans, J. H. C., Drost, N., et al. (2018). PCR-GLOBWB 2: A 5 arcmin global hydrological and water resources model. *Geoscientific Model Development*, *11*(6), 2429–2453. <https://doi.org/10.5194/gmd-11-2429-2018>
- Tapley, B. D., Watkins, M. M., Flechtner, F., Reigber, C., Bettadpur, S., Rodell, M., et al. (2019). Contributions of GRACE to understanding climate change. *Nature Climate Change*, *9*(5), 358–369. <https://doi.org/10.1038/s41558-019-0456-2>
- Tian, Z., Fan, Y., Wang, K., Zhong, H., Sun, L., Fan, D., et al. (2021). Searching for “Win-Win” solutions for food-water-GHG emissions tradeoffs across irrigation regimes of paddy rice in China. *Resources, Conservation and Recycling*, *166*, 105360. <https://doi.org/10.1016/j.resconrec.2020.105360>
- Tiwari, V. M., Wahr, J., & Swenson, S. (2009). Dwindling groundwater resources in northern India, from satellite gravity observations. *Geophysical Research Letters*, *36*(18), L18401. <https://doi.org/10.1029/2009GL039401>
- Tong, J., Qiang, Z., Deming, Z., & Yijun, W. (2006). Yangtze floods and droughts (China) and teleconnections with ENSO activities (1470–2003). *Quaternary International*, *144*(1), 29–37. <https://doi.org/10.1016/j.quaint.2005.05.010>
- Torrence, C., & Compo, G. P. (1998). A practical guide to wavelet analysis. *Bulletin of the American Meteorological Society*, *79*(1), 61–78. [https://doi.org/10.1175/1520-0477\(1998\)079<0061:APGTWA>2.0.CO;2](https://doi.org/10.1175/1520-0477(1998)079<0061:APGTWA>2.0.CO;2)
- Wang, Y., Sun, Z., Wu, Q., Fang, J., & Jia, W. (2022). Spatio-temporal variability of terrestrial water storage in the Yangtze River basin: Response to climate changes. *Geodesy and Geodynamics*, *14*(3), 201–211. <https://doi.org/10.1016/j.geog.2022.11.006>
- Watkins, M. M., Wiese, D. N., Yuan, D.-N., Boening, C., & Landerer, F. W. (2015). Improved methods for observing Earth's time variable mass distribution with GRACE using spherical cap mascons. *Journal of Geophysical Research: Solid Earth*, *120*(4), 2648–2671. <https://doi.org/10.1002/2014JB011547>
- Williams, A. P., Cook, B. I., & Smerdon, J. E. (2022). Rapid intensification of the emerging southwestern North American megadrought in 2020–2021. *Nature Climate Change*, *12*(3), 232–234. <https://doi.org/10.1038/s41558-022-01290-z>
- Willmott, C. J., & Matsuura, K. (1995). Smart interpolation of annually averaged air temperature in the United States. *Journal of Applied Meteorology*, *34*(12), 2577–2586. [https://doi.org/10.1175/1520-0450\(1995\)034<2577:SIOAAA>2.0.CO;2](https://doi.org/10.1175/1520-0450(1995)034<2577:SIOAAA>2.0.CO;2)
- Yang, P., Zhang, S., Xia, J., Zhan, C., Cai, W., Wang, W., et al. (2022). Analysis of drought and flood alternation and its driving factors in the Yangtze River basin under climate change. *Atmospheric Research*, *270*, 106087. <https://doi.org/10.1016/j.atmosres.2022.106087>
- Yang, S., Wu, B., Zhang, R., & Zhou, S. (2013). Relationship between an abrupt drought-flood transition over mid-low reaches of the Yangtze River in 2011 and the intraseasonal oscillation over mid-high latitudes of East Asia. *Acta Meteorologica Sinica*, *27*(2), 129–143. <https://doi.org/10.1007/s13351-013-0201-0>
- Yang, X., Zhang, M., He, X., Ren, L., Pan, M., Yu, X., et al. (2020). Contrasting influences of human activities on hydrological drought regimes over China based on high-resolution simulations. *Water Resources Research*, *56*(6), e2019WR025843. <https://doi.org/10.1029/2019WR025843>
- Yin, W., Yang, S., Hu, L., Tian, S., Wang, X., Zhao, R., & Li, P. (2022). Improving understanding of spatiotemporal water storage changes over China based on multiple datasets. *Journal of Hydrology*, *612*, 128098. <https://doi.org/10.1016/j.jhydrol.2022.128098>
- Yin, Y., Xu, Y., & Chen, Y. (2009). Relationship between flood/drought disasters and ENSO from 1857 to 2003 in the Taihu Lake basin, China. *Quaternary International*, *208*(1–2), 93–101. <https://doi.org/10.1016/j.quaint.2008.12.016>
- Yu, X., Wang, Z., Zhang, H., & Zhao, S. (2019). Impacts of different types and intensities of El Niño events on winter aerosols over China. *Science of the Total Environment*, *655*, 766–780. <https://doi.org/10.1016/j.scitotenv.2018.11.090>
- Yuan, Y., Gao, H., Li, W., Liu, Y., Chen, L., Zhou, B., & Ding, Y. (2017). The 2016 summer floods in China and associated physical mechanisms: A comparison with 1998. *Journal of Meteorological Research*, *31*(2), 261–277. <https://doi.org/10.1007/s13351-017-6192-5>
- Zhai, P., Yu, R., Guo, Y., Li, Q., Ren, X., Wang, Y., et al. (2016). The strong El Niño of 2015/16 and its dominant impacts on global and China's climate. *Journal of Meteorological Research*, *30*(3), 283–297. <https://doi.org/10.1007/s13351-016-6101-3>
- Zhang, D., Zhang, Q., Werner, A. D., & Liu, X. (2016). GRACE-based hydrological drought evaluation of the Yangtze River basin, China. *Journal of Hydrometeorology*, *17*(3), 811–828. <https://doi.org/10.1175/JHM-D-15-0084.1>
- Zhang, T., Hoell, A., Perlwitz, J., Eischeid, J., Murray, D., Hoerling, M., & Hamill, T. M. (2019). Towards probabilistic multivariate ENSO monitoring. *Geophysical Research Letters*, *46*(17–18), 10532–10540. <https://doi.org/10.1029/2019GL083946>
- Zhang, Z., Chao, B. F., Chen, J., & Wilson, C. R. (2015). Terrestrial water storage anomalies of Yangtze River basin droughts observed by GRACE and connections with ENSO. *Global and Planetary Change*, *126*, 35–45. <https://doi.org/10.1016/j.gloplacha.2015.01.002>
- Zhao, M., Geruo, A., Velicogna, I., & Kimball, J. S. (2017). A global gridded dataset of GRACE Drought Severity Index for 2002–14: Comparison with PDSI and SPEI and a case study of the Australia Millennium Drought. *Journal of Hydrometeorology*, *18*(8), 2117–2129. <https://doi.org/10.1175/JHM-D-16-0182.1>